UNIVERSITY OF CALIFORNIA SAN DIEGO

“Genetic and Pharmacological Manipulation of Heparan Sulfate Accelerates Wound Healing”

A thesis submitted in partial satisfaction of the
requirements for the degree Master of Science

in

Chemistry

By

Raquel Jewel Riley

Committee in charge:

Professor Jeffrey Esko, Chair
Professor Kamil Godula, Co-Chair
Professor Michael Burkart

2020

The thesis of Raquel Jewel Riley is approved, and it is acceptable in quality and form for publication on microfilm and electronically.

Co-Chair

Chair

University of California San Diego

2020

TABLE OF CONTENTS

Signature Page iii

Table of Contents iv

List of Figures v

Acknowledgements vii

Abstract of Thesis viii

Introduction 1

Chapter 1: Genetic and Pharmacological Deficiency in Heparan Sulfate Accelerates Dermal Wound Closure 10

Chapter 2: Genetic and Pharmacological Deficiency in Heparan Sulfate Accelerates Cartilage Regeneration 26

Part I: *K14-Cre^{ER}; Ext1$^{f/f}$; mTmG* Mouse Model 27

Part II: Xyloside Mouse Model 38

Part III: *Prrx- Cre^{ER} Ext1$^{+/-}$Ext2$^{+/-}$ Luc$^{/Luc}$* Mouse Model 53

Conclusion 67

References 70

LIST OF FIGURES

Figure 1.1- Diagram of 6mm punch dorsal cutaneous wounding scheme 19

Figure 1.2- Photos of 6mm wounds on live animals; Day 0-10; Wildtype compared to *Ext1*$^{+/-}$*Ext2*$^{+/-}$ 20

Figure 1.3- Quantification of dorsal cutaneous wound closure over time from the mice in Figure 1.2 21

Figure 1.4- Histology of Wildtype and *Ext1*$^{+/-}$*Ext2*$^{+/-}$ wounds; Day 0-12; Staining with Hematoxylin & Eosin and Ki67 22

Figure 1.5- Quantification of Figure 1.3. Cell proliferation at Day 14 post-wound shown with Hematoxylin & Eosin and Ki67 staining 23

Figure 1.6- Graph of quantification of levels of heparan sulfate in dermal cutaneous wounds 24

Figure 1.7- Graph of the quantification of levels of chondroitin sulfate in dermal cutaneous wounds 25

Figure 2.1- Diagram of 2mm ear punch wounding scheme in *K14 Cre*^{ER} *Ext1*$^{f/f}$ *mTmG* mouse model 34

Figure 2.2- Photos of 2mm ear wounds on live animals; Day 0-25; *K14 Cre*$^{+}$ *Ext1*$^{f/f}$ *mTmG* compared to *K14 Cre*$^{-}$ *Ext1*$^{f/f}$ *mTmG* 35

Figure 2.3- Graph of the quantification of 2mm ear wound closure of *K14 Cre*^{ER} *Ext1*$^{f/f}$ *mTmG*; Day 0-49 36

Figure 2.4- Histology of *K14 Cre*$^{-}$*Ext1*$^{f/f}$ *mTmG* and *K14 Cre*$^{+}$*Ext1*$^{f/f}$ *mTmG* 2mm ear punch wound closure with trichrome staining 37

Figure 3.1- Scheme of NMX synthesis 47

Figure 3.2- Photos of 6mm wounds on live animals; Day 0-10; Wildtype compared to wildtype given 1mM of NMX *ad libitum* as a drinking source 48

Figure 3.3- Quantification of dorsal cutaneous wound closure over time from the mice in Figure 3.2 49

Figure 3.4- Diagram of 2mm ear punch wounding scheme in wildtype xyloside mouse model 50

Figure 3.5- Photos of 2mm ear wounds on live Wildtype animals orally given water, NMA, or NMX; Day 0-49..... 51

Figure 3.6- Graph of the quantification of 2mm ear wound closure of Wildtype mice orally treated with water, NMA, or NMX; Day 0-49 52

Figure 4.1- Diagram of *Prrx-Cre^{ER} Rosa26-LSL-Luc* reporter system 61

Figure 4.2- Diagram of 2mm ear punch wounding scheme in *Prrx-Cre^{ER} Rosa26-LSL-Luc* mouse model 62

Figure 4.3- Photos of 2mm ear wounds on live animals using IVIS Imaging for luminescence (photons/second); Day 0-7. Various genotypes tested: *Luc$^{/Luc}$*, *Ext1$^{+/-}$ Luc$^{/Luc}$*, *Cre^{+} Luc$^{/Luc}$*, *Cre^{+} Ext1$^{+/-}$ Luc$^{/Luc}$*, *Cre^{+} Ext1$^{+/-}$ Ext2$^{+/-}$ Luc$^{/Luc}$* ... 63

Figure 4.4- Photos of 2mm ear wounds on live animals using IVIS Imaging for luminescence (photons/second); Day 0-28. F1, F2: *Cre^{+} Luc$^{/Luc}$*; F4, F5: *Cre^{+} Ext1$^{+/-}$ Ext2$^{+/-}$ Luc$^{/Luc}$*; F6: *Luc$^{/Luc}$* 64

Figure 4.5- Graph of the quantification of ROI data (photons/second) collected from IVIS Imaging; Day 0-28..... 65

Figure 4.6- Graph of the quantification of 2mm ear wound closure of *Prrx* mouse model; Day 0-28 66

ACKNOWLEDGEMENTS

I would like to acknowledge Professor Jeffrey Esko for his support as the chair of my defense committee. Through multiple drafts and many long nights, his guidance has proved to be invaluable. I have truly enjoyed my time in the Esko Lab.

I would also like to thank the other members of my committee, Professor Kamil Godula and Professor Michael Burkhart. They have given me great insight and I am appreciative of their feedback and mentoring.

In addition, I would like to acknowledge Anne Phan, PhD, without whom my research would have never been possible. It is her support that guided me in the right direction, and I cannot thank her enough for all that she has taught me.

I would like to thank my mom and sister, Candace and Haley Riley, for being my family and supporting me through all my ups and downs. I know it has been a long road for all of us and I genuinely want to thank both of them for their love, patience, and understanding.

Chapter 1 and 2, in part has coauthored and been executed by Anne Phan. Her previous studies have been incorporated into this thesis with her permission and I thank her and others for allowing me to continue their incredible work. The thesis author is the primary author of these chapters.

Chapter 2, part II, in part is coauthored and has been executed by Bryce Timm and Steven Verespy from the Kamil Godula lab. Without their work, this mouse model would not have been possible. The thesis author is the primary author of this chapter.

ABSTRACT OF THE THESIS

"Genetic and Pharmacological Manipulation of Heparan Sulfate Accelerates Wound Healing"

by

Raquel Jewel Riley

Master of Science in Chemistry

University of California San Diego, 2020

Professor Jeffrey Esko, Chair
Professor Kamil Godula, Co-Chair

The objective of this thesis was to test various mouse models to determine a genetic or pharmacological method of accelerating the wound healing process. Specifically, we were trying to determine a mouse model that could result in wound regeneration without scarring. To achieve this, we developed different methods to knockdown heparan sulfate (HS) expression because of its role in the three steps of the wound repair process, inflammation, proliferation, and remodeling.

First, we investigated the phenotypic effect on healing with *Ext1*$^{+/-}$*Ext2*$^{+/-}$ gene mutation in C57BL/6 mice. *Ext1*$^{+/-}$*Ext2*$^{+/-}$ mutation has proven to enhance wound healing significantly, observing a difference after two days post wound, whereas the wildtype lagged significantly. *In vivo* HS expression in the skin of wildtype and *Ext1*$^{+/-}$*Ext2*$^{+/-}$ mice, resulted in a knockdown of more than 50%. For the first time, chondroitin sulfate expression in mouse skin was determined, ranging between 50-60 μg/gram of tissue. Second, *K14-Cre*^{ER}*Ext1*$^{f/f}$ mice showed significant wound repair compared to the control, resulting in 53.4% to 22.7% wound healing, respectively. Not only did the *K14-Cre*$^{+}$*Ext1*$^{f/f}$ mice have an accelerated repair rate, but there were also the beginning stages of regeneration. Thirdly, although NMX enhanced wound healing significantly in dorsal wounds, it was not well translated to the wound repair in the ear. The addition of the two aromatic rings bound to the xyloside in NMX allowed for more efficient priming of HS because it created an optimal planar configuration. Lastly, while the *Prrx-Cre*^{ER} *Rosa26-LSL Luc* mouse model did not indicate enhanced wound healing, it did provide a better understanding on how cartilage repair occurs. Through IVIS imaging we could track the increase of *Prrx* expression after wounding. Indicating that after initial wounding *Prrx-Cre*^{ER} was recruited to the wound site to assist in the repair process. The elevated expression stayed consistent over four weeks demonstrating that the wound healing occurs for an extended period of time. Overall, the investigation into the discovery of a mammalian model for wound regeneration caused by the manipulation of HS expression, genetically and pharmacologically, did result in some models that had enhanced and accelerated the wound repair and regeneration.

INTRODUCTION

Over the years, many have tried to study wound regeneration and wound repair, most of which were either done *in vitro* or used various species of amphibians. To be able to understand how species like these are able to regenerate functional limbs after amputation could give great insight into the mechanisms used. However, understanding the mechanisms is fruitless if it cannot be applied in mammals and specifically humans. In this thesis, we will be exploring different ways to induce regeneration or accelerate wound repair in mice. We will dive deep into different variables, researching both cutaneous and cartilage wound healing. In addition, testing whether diverse genetics result in increased, decreased, or no change in wound healing. Other methods of treatment, like oral consumption or topical treatment, could be beneficial in this study.

Probably the most important aspect to differentiate in this study is to compare wound regeneration to wound repair. There is a significant difference between regeneration and repair. Regeneration is defined as the gross replacement and rebuilding of mature tissue that is able to achieve normal function and architecture (Clark, et al., 1998). It has been discovered that the inflammatory response system plays a key role in regenerative healing with the help from the proinflammatory molecule COX-2. Regeneration requires the recruitment of stem cells and differentiation cells because these cells can split, producing the replacement cells and are directed to form the correct functional structures (Gourevitch, et al., 2014). In addition, inflammation will contribute other inflammatory immune cells like neutrophils, basophils, eosinophils, platelets, and monocytes.

Regeneration has been observed in various species. Some studies have shown that mice can regrow the tips of their digits and closure of hole punch wounds in the ears of mice and rabbits (Goss, et al., 1975; Borgens, 1982; Clark, et al., 1998). Others have studied antlerogenesis, which

is the regeneration of antlers after they are lost on many species of deer (Goss, 1970; Chunyi, et al., 2013). While, amphibians and fishes are probably the most often studied for regeneration, they have shown to be greatly capable of regenerating organs or limbs (Kyritsis, et al., 2012; Phan, et al., 2015). As far as regenerative research has come in the past few decades, there has been little clinical relevance that could be applicable to humans.

On the other hand, wound repair occurs in all living organisms and we see it every day, from injured animals in the wild to children scraping their knees at the park. Wound repair is defined as the replacement of injured or destroyed tissue with new tissue. Once an injury occurs, the natural response within the system is to stop the bleeding. A clot will be formed at the site of the wound and consists of platelets, thrombin, collagen, and fibronectin, which in turn caused the activation of cytokines and specific growth factors (Barrientos, et al., 2008). This release is the first step of wound repair, inflammation. Wound repair or healing induces molecules with chemotactic activity to be produced, forcing the migration of fibroblasts and keratinocytes to the site of the wound (Williams, 1998; Nascimento, et al., 2006; Davis, et al., 2007). Fibroblasts are critical in the synthesis of the extracellular matrix (ECM) proteins and collagen which provide the beginning structures of tissue (Murray, et al., 2009). After the recruitment of fibroblasts, granulation tissue begins, causing macrophages and neutrophils to cover the majority of the wound (Im and Kim, 2009). Neutrophils are white blood cells that are a part of the innate immune system that help protect the species wounded fight off any infection that may occur at the site of the injury. Macrophages are also specified cells involved in detecting and combatting infection, but more importantly, macrophages release chemical signals to recruit a surge of more fibroblasts and collagen (Im and Kim, 2009).

After the recruitment of fibroblasts, granulation tissue begins the proliferation stage of wound healing. Keratinocytes, that are mainly located in the epidermis, multiply and migrate to the site of the wound, beginning to cover the forming matrix of granulation tissue, resulting in new epithelialization (Eming, et al., 2007). Macrophages then cause the induction of FGF-2 and TGFα, fibroblast growth factors (Clark, et al., 1998; Williams, 1998; Gourevitch, et al., 2014). These growth factors can then stimulate mitogenesis, cell differentiation, and angiogenesis (Im and Kim, 2009). As the fibroblasts numbers increase, so does the granulation tissue resulting in the production of collagen I and III, as well as proteoglycans and glycosaminoglycans (GAGs). The collagen forms in a disorganized manner, and the synthesis of the extracellular matrix increases. Some fibroblasts are then transformed into myofibroblasts that then assists in wound contraction (Im and Kim, 2009). The last stages in proliferation of wound healing are the deposition of collagen and GAGs to the basement membrane and the induction of angiogenesis, which in turn leads to the formation of scar tissue and strengthening the wound until complete closure (Clark, et al., 1998; Williams, 1998; Im and Kim, 2009).

Even though the biology and mechanisms of wound regeneration and repair are generally understood, there is still motivation to discover a way to enhance the rate and quality of healing. The past three decades scientists have been breaking ground in wound regeneration and repair. The most notably was the paper "A New Murine Model of Mammalian Wound Repair and Regeneration" written in 1998, to which was the first to demonstrate complete wound regeneration in mice (Clark, et al.). They were able to document cartilaginous wound closure in Murphy Roths Large (MRL) mice. A 2mm diameter through-and-through ear hole punch was made in the center of the MRL and control C57BL/6 mice ears and tracked the wound closure over time. The wounds had full closure and were determined to have restored normal function and architecture. The

histology of the wound healing showed all the signs of regeneration with new cartilage being formed in the ear (Clark, et al., 1998). These experiments done in 1998 have outlined the projects for this thesis and the principal take away from the MRL mouse model results is that regeneration is possible in higher mammals. Throughout this thesis, we will be attempting to repeat the regenerative results in different mouse models.

The results from the MRL mouse model paved a path for regenerative research, but the next problem to figure out was the mechanisms behind the wound healing. In 2014, a group published a paper to do just that. "Inflammation and Its Correlates in Regenerative Wound Healing" looked into the role of inflammation in both wound regeneration and wound repair (Gourevitch, et al., 2014). In the paper, it was confirmed the 2mm ear hole punch closure is in fact an example of mammalian regenerative healing. Then, inflammation was investigated to see how it plays a role in healing. The MRL mice presented increased inflammation as compared to the C57BL/6 mice, which in turn caused the release of the proinflammatory molecule, COX-2. Stem cells and differential cells migrate to the wound and begin remodeling. It was concluded that within remodeling the cells became more stable and have reduced cytotoxicity (Canhamero, et al., 2014; Gourevitch, et al., 2014). With an amplified HIF-1α expression and increased angiogenesis, development of new blood vessels, the MRL mice were able to obtain full closure of the through-and-through wound with minimal scarring (Gourevitch, et al., 2014). Therefore, inflammation plays a vital role in both wound repair and regeneration, but also gives insight on how regeneration in mammals could be manipulated.

One way to increase the rate and quality of wound healing can be through the administration of drugs. "Drug-induced regeneration in adult mice", a paper published in 2015, describes how an important oxygen-related protein known as HIF-1α can aid in the healing process

(Zhang, et al.). HIF-1α is easily hydroxylated in the cytoplasm of the cell. HIF-1α must then form a complex with HIF-1β in the nucleus of the cell and induces transcription. The complex will bind directly to the DNA at a given promoter such that it is able to regulate and enhance transcription of more than 100 genes (Semenza, 2001; Weidemann and Johnson, 2008). The enhanced transcription results in the increased expression of proteins and other small molecules that assist in angiogenesis. Vascular endothelial growth factor (VEGF) is an important growth factor along with urokinase-type plasminogen activator receptor (uPAR) and lactate dehydrogenase (LDH) that promotes tissue restoration and glycolytic metabolism (Zhang, et al., 2014).

Since HIF-1α is easily hydroxylated by the prolyl hydroxylase enzyme (PHD), the researchers were able to create a drug induced mouse model to test the importance of HIF-1α (Tan, et al., 2005; Zhang, et al., 2015). PHDs control the synthesis and distribution of collagen in fibroblasts, that eventually leads to wound healing with minimal scar tissue forming (Zhang, et al., 2009). The mouse model had a drug-induced inhibitor of PHDs that allowed HIF-1α to stabilize in the cytoplasm and bind HIF-1β more readily; the inhibitor is 1,4-dihydrophenonthrolin-4-1-3-carboxylic acid (1,4-DPCA). 1,4-DPCA was made into a drug/hydrogel that was subcutaneously injected into the non-regenerative mice and proven to increase HIF-1α expression and stabilization (Zhang, et al., 2015). Although MRL mice exhibited complete wound closure in only seven days, the mice injected with the 1,4-DPCA inhibitor reached full wound closure in 35 days with minimal scarring. Thus, this led to the conclusion that it is possible to create a drug-induced mammalian wound healing process that results in rapid repair and regeneration (Zhang, et al., 2015).

To take a different approach to the wound healing model, some attempted to mediate regeneration in axolotl by manipulating the levels of heparan sulfate. In 2015, a group was able to show heparan sulfate dependent regeneration on many levels (Phan, et al.). Although the

regeneration experiments were completed on axolotl, amphibians known for limb regeneration, the goal was to isolate a specific gene or set of genes that would result in increased wound regeneration. Growth factors are required to initiate regeneration and the presence of heparan sulfate was found to be needed for signaling (Rapraeger, et al., 1991). Heparan sulfate acts as a cofactor and is part of the ECM, where the cell-surface heparan sulfate proteoglycans in the ECM have specific binding sites for the growth factors involved (Sarrazin, et al., 2011). It was reported that heparan sulfate located in the ECM induces pattern formation and is involved in the encoding of position-specific migration and differentiation of cells (Phan, et al., 2015). Therefore, heparan sulfate expression is a key component to wound regeneration and repair.

Dr. Jeffrey Esko, a professor at the University of California San Diego and a committee member of this thesis, focuses his team's research around the proteoglycan heparan sulfate and other types of glycosaminoglycans. Glycosaminoglycans are defined as highly sulfated linear polysaccharides characterized by negatively-charged repeating disaccharide units. Most glycosaminoglycans are comprised of a hexosamine and an uronic acid (Im and Kim, 2009). The two major hexosamines are D-glucosamine and D-galactosamine, which are compounds containing a six-carbon sugar with a NH_2 attached. D-glucuronic acid and L-iduronic acid are the primary uronic acid compounds, which contains an additional OH group on a six-carbon sugar (Im and Kim, 2009). The majority of glycosaminoglycans are located at the cell surface covalently bound to proteins, in the extracellular matrix, and the basement membrane (Au-Yeung, et al., 2011). Heparan sulfate, heparin, chondroitin sulfate, dermatan sulfate, hyaluronic acid, and keratan sulfate are all glycosaminoglycans that are well studied.

Glycosaminoglycans play key roles in many biological functions. Heparin is a highly sulfated GAG that is widely used as an anticoagulant, used often as a blood thinner medication to

prevent blood clots in patients by forming a complex with antithrombin III (Im and Kim, 2009). Many cell surface glycosaminoglycans, such as heparan sulfate and chondroitin sulfate, are targets for viruses and microbial pathogens. They will act as a binding site for the pathogen and potentially aid in the invasion of the pathogen into the host (Jinno and Park, 2014). Additionally, glycosaminoglycans modulates cell signaling, allowing GAGs to participate in a broad range of biochemical processes (Afratis, et al., 2012). However, when in reference to wound regeneration and repair, heparan sulfate and chondroitin sulfate are the glycosaminoglycans that present the greatest role in wound healing.

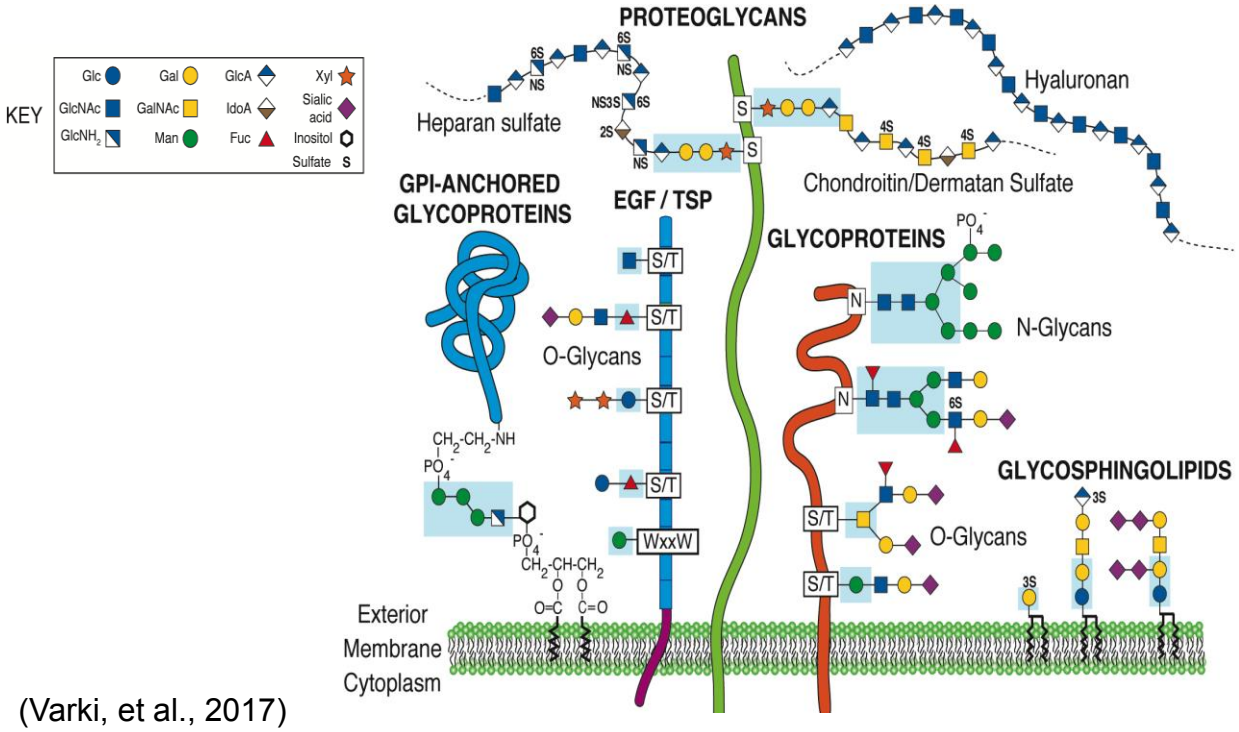

(Varki, et al., 2017)

Heparan sulfate is sulfated polysaccharide composed of repeating disaccharides glucuronic acid (GlcA) and *N*-acetyl-D-glucosamine (GlcNAc). Heparan sulfate plays numerous roles throughout the wound healing process, but most notably is its role a cofactor for FGF-receptor binding (Landau, et al., 2001). These growth factors then stimulate cell proliferation, cell differentiation, and angiogenesis. Heparan sulfate also helps to maintain blood volume and

protease activity after an injury by interceding coagulation processes and angiogenesis of epithelial cells at the surface of the wound (Shriver, et al., 2002; Zhou, et al., 2004). Heparin, as a natural blood thinner, increases capillary circulation which also promotes angiogenesis and leads to enhanced wound healing and acts as an anti-inflammatory agent (Cen, et al., 2000; Saliba, 2001).

Chondroitin sulfate on the other hand consists of the repeating disaccharides D-glucuronic acid (GlcA) and *N*-acetyl-D-galactosamine (GalNAc) and can be sulfated at three specific carbons of the given disaccharide. Aggrecan, versican, brevican, and neurocan are some of the chondroitin sulfate proteoglycans and all contribute to development of the central nervous system, growth factor signaling, and wound repair (Zou, et al., 2009). Chondroitin sulfate is a cofactor that binds to FGF-2 and then activates a focal adhesion growth factor (FAK) that leads to increased cell proliferation and cell migration (Zou, et al., 2004). Furthermore, the enzyme chondroitin sulfate synthase 1 (CHSY1) is one of many enzymes that biosynthesizes chondroitin sulfate. It was found in previous literature that if CHSY1 expression was downregulated in fibroblasts that the expression of a cysteine-aspartic acid protease caspase 1 (CASP1) also decreased (Au-Yeung, et al., 2011). CASP1 plays a role in both cell proliferation and cell migration, thus decreasing the expression would slow the wound healing process. Therefore, CHSY1 enzyme expression could be influenced to upregulate CASP1 expression and increase the wound repair time (Au-Yeung, et al., 2011).

The objective of this thesis was to test a series of mouse models to determine a genetic or pharmacological method of accelerating the wound healing process. Specifically, we were trying to determine if a mouse model other than the MRL could result in wound regeneration without scarring. First, we will look at dorsal cutaneous wound repair and compare different mouse models for rate of wound closure, such that the specific genotypes $Ext1^{+/-}$ and $Ext2^{+/-}$ were investigated

due to their ability to knockdown of heparan sulfate expression. Additionally, we will attempt to quantify the *in vivo* heparan sulfate and chondroitin sulfate levels in the dorsal cutaneous tissue. The back half of this thesis investigates genetic and pharmacological manipulation of heparan sulfate on cartilage regeneration and repair. Overall, we are trying to discover a mammalian model of wound regeneration and determine other methods, genetically and pharmacologically, to enhance and accelerate the wound repair process of inflammation, proliferation, and remodeling.

Chapter 1

Genetic and Pharmacological Manipulation of Heparan Sulfate Accelerates Dorsal Cutaneous Wound Closure

INTRODUCTION

Heparan sulfate and chondroitin sulfate are vital glycosaminoglycans to everyday biological functions. Heparan sulfate is sulfated polysaccharide composed of repeating disaccharides glucuronic acid (GlcA) and *N*-acetyl-D-glucosamine (GlcNAc) (Sarrazin, et al., 2011). Activation of glycosyltransferase induces elongation of the polysaccharide which adds to the reducing end of the chain β1,4 -GlcA and then α1,4- GlcNAc as repeating units (Busse-Wicher, et al., 2014; Varki, et al., 2017). Heparan sulfate plays numerous roles throughout the wound healing process, but most notably is its role a cofactor for FGF-receptor binding which then stimulates cell proliferation, cell differentiation, and angiogenesis (Landau, et al., 2001). Chondroitin sulfate on the other hand is contains of the repeating disaccharides D-glucuronic acid (GlcA) and *N*-acetyl-D-galactosamine (GalNAc) and can be sulfated at three specific carbons of the given disaccharide. Chondroitin sulfate also contributes to development of the central nervous system, growth factor signaling, and wound repair (Zou, et al., 2009).

Since both of these glycosaminoglycans showed an influence on wound repair and cell proliferation, we decided to manipulate the expression of heparan sulfate in an *Ext* heterozygous mouse model. *Ext1* and *Ext2* have both demonstrated that they are required for the biosynthesis of heparan sulfate and both are needed for the elongation of heparan sulfate chains (Wei, et al., 2000; Busse-Wicher, et al., 2014). The protein Ext1 can act as a GlcNAc transferase and Ext2 can also act as a glycosyltransferase allowing GlcNAc and GalNAc to form α-linkages (Kim, et al., 2001; Okada, et al., 2010; Busse-Wicher, et al., 2014). It has been noted that if *Ext1* gene is knocked out completely in mice, the $Ext1^{-/-}$ die at embryo day 8.5, but if the mice are only knocked down to heterozygous $Ext1^{+/-}$ the mice show no phenotypical differences compared to the $Ext1^{+/+}$ mice (Lin, et al., 2000; Zak, et al., 2011). Mice that were $Ext1^{+/-}$ were found to have heparan sulfate

expression levels halved, resulting in a knockdown of HS rather than a knockout (Lin, et al., 2000). The goal of this mouse model is to determine if the reduction of heparan sulfate has an effect on wound healing, and both *Ext1*$^{+/-}$ and *Ext2*$^{+/-}$ were observed as well as a double heterozygous *Ext1*$^{+/-}$ *Ext2*$^{+/-}$.

MATERIALS AND METHODS

Materials. Nair™ was used for hair removal. Superfrost Plus Microscope slides were purchased from Fisher Scientific (Cat. #1255015). Ki67 antibody was purchased from Bio-Rad (Cat. #HCA053). 10% buffered formalin was purchased from Fisher Scientific (Cat. #SF93-4). Gill II hematoxylin and Eosin were purchased from Surgipath (Cat. #01522; #01602). Scotts Tap water, also known as Shandon bluing reagent, and Citrosol were purchased from Fisher Scientific (Cat. #CS410-4; #22-143-975). The mounting media, Cytoseal 60 was purchased from VWR (Cat. # 48212-14) and the glass coverslips were also from Surgipath (Cat. #00145).

Proteinase K was used for the digestion of the skin tissue and purchased from Worthington Biochemical Corporation (Cat. #LS004222). The 0.45µm PES Nalgene Syringe filter was purchased from Thermo Fisher Scientific (Cat. #194-2545). The DEAE-Sephacel and PD-10 columns were purchased from GE Healthcare (Cat. # 17-0500-01; #17-0851-01). The 10mL Bio-Rad poly-prep chromatography columns were purchased from Bio-Rad (Cat. #731-1550). Chondroitinase ABC protease free 10U/vial (ChABC) was purchased from Amsbio (Cat. #AMS.E1028-10). Heparan lyase was purchased from Iduron (Cat. #HL01). Aniline and dimethyl sulfoxide (DMSO) were purchased from Sigma (Cat. #242284; #276855). Glacial acetic acid was purchased from Fisher Scientific (Cat. #A35-500).

Wounding and Imaging. A series of C57BL/6 wildtype mice and genetically modified *Ext1*$^{+/-}$ *Ext2*$^{+/-}$ mice were shaved and treated with Nair to remove all hair from the back of the mice at

P54. At P56, the mice were subject to two 6mm, in diameter, dorsal cutaneous punch wounds. Each wound on the mice was photographed everyday over a course of 14 days to track the wound closure and healing.

Histology. At the end of the wound healing process, the mice were sacrificed. The areas that were affected were collected for histology for each genotype. The dorsal skin was collected from unwounded genotypes, one day post-wound, and 14 days post-wound. The skin was embedded in Paraffin such that it would be cut into 5µm sections by a rotary microtome in a sagittal direction in reference to the skin. The samples were then placed on positively charged glass slide and let to dry overnight. The slides were covered in a 1:100 dilution of Ki67 antibody for 1 hour at room temperature. The slides were then imaged to show cell proliferation on the NanoZoomer digital slide scanner.

The slides were then subject to Hematoxylin & Eosin (H&E) staining. H&E was completed by first fixing the slides in 10% neutral buffered formalin for 30 minutes, rinsed in deionized (DI) water, washed in Gill II Hematoxylin for 4 minutes, rinsed again in DI water, washed in Scotts Tap water for 1 minute, rinsed with DI water, dipped once in 95% ethanol, washed in Eosin for 4 minutes, rinsed with DI water, washed in 95% ethanol for 1 minutes, washed in 100% ethanol, and soaked in Citrisolv in a total of 6 minutes. Finally, permanent mounting media was used to seal a coverslip to the slide and let dry until imaging. Wound size quantification was done using ImageJ programming.

GAG Quantification Analysis. A cohort of C57BL/6 wildtype and genetically modified *Ext1*$^{+/-}$ *Ext2*$^{+/-}$ mice were shaved and Nair was applied on day P55 and sacrificed on P56. A 30x15 mm section of skin was cut out from the dorsal area of the mouse. The wet weight was recorded, and the samples were finely minced with micro-scissors and 4mL of DEAE pre-wash buffer was added

to each sample. 200µL of 20mg/mL of Proteinase K was added to each vial, then each vial was rotated at 50°C overnight. The Proteinase K addition was repeated twice more over a total of 3 days and 600µL. The Proteinase K was then deactivated by placing in 100°C for 5 minutes. Each sample was then filtered using a 0.45µM PES syringe filter.

The GAG sample was the purified over 0.5 mL DEAE columns and desalted over PD10 columns. The samples were then spun down, froze to -80°C, and lyophilized until dry. The dried samples were resuspended in 1mL of DI water and 100µL and 200µL of the sample was enzymatically digested with ChABC and Hep Lyase I/II/III respectively overnight at 37°C. The samples were then dried via speed vac.

The samples were then aniline tagged with 17µL of aniline and 17µL of a reductant composed of $NaCNBH_4$, DMSO, and glacial acidic acid. The samples were vortexed and incubated overnight at 37°C. The samples were then dried via speed vac and prepared for LC/MS GAG analysis. This was done by resuspending the samples in 16µL of Mass Spec-grade water. Then 5µL were transferred to a MS vial along with 3µL of LC/MS water, 1µL of 10x LC/MS buffer, and 1µL of standard respective to either the CS or HS digestion. 4µL of the vial was injected for analysis.

RESULTS

The knock down or heparan sulfate has shown to have a positive effect on wound healing in axolotl models in previous literature. The primary focus of this chapter was to investigate if these findings could be extended to mammals, in particular mice. To study this problem, we developed a wound model in which two large wounds were made in the dorsal cutaneous area of the mice. The aim for this project was to investigate the phenotypic effect on regeneration of the $Ext1^{+/-}Ext2^{+/-}$ gene mutation in C57BL/6 mice. Previous work has shown increased wound closure

in dorsal cutaneous wounds in *Ext1*$^{+/-}$*Ext2*$^{+/-}$ mice. The mice received two 6-mm diameter dorsal cutaneous punch biopsies (**Figure 1.1**). The mice were imaged on the day of wounding and for two weeks following the punch biopsy. There was a significant increase in the rate of wound closure as compared to the control wildtype C57BL/6 mice already manifests by day two post wound (**Figure 1.2**). By day four post wound, the *Ext1*$^{+/-}$*Ext2*$^{+/-}$ wounds began to scab and almost completely healed by day ten post wound, whereas the wildtype lagged significantly. The wound area was quantified, and the double het mutant had increased wound closure compared to the single het mutants and wildtype (**Figure 1.3**). Although, as seen before, the knockdown of heparan sulfate was almost the same across all the mutants. One reason only the double het mutant had enhanced healing is that the GAG analysis consisted of the whole tissue including the extracellular matrix. Wound closure may only depend on a particular subset of cells and could give rise to these results.

To investigation of how this phenotype came about, the wounds at various time points were studied immunohistochemically (**Figure 1.4**). Mice of different genotypes were sacrificed at the time of wounding, one day post wounding, and fourteen days post wounding. In panel A of the figure, there is no physical difference in cell types and hair follicle cycles in mutant and wildtype mice prior to wounding. The hair follicles are indicated by the black arrow head in panel A, and the layers of the skin are broken down into three main sections. The epidermis is the outer most layer of the skin labeled "E"; the dermis is the layer of skin that contains most of the hair follicles, sweat glands, and sebaceous glands, indicated as "D". The largely pink areas identified in section "SM" of the skin depicts the skeletal muscle. After 1 day, the *Ext1*$^{+/-}$*Ext2*$^{+/-}$ skin showed increased cell proliferation around the wound. The thickness of the wound site almost doubled in size compared to the control. After 14 days, the wound area is significantly smaller in diameter in the mutant. The wound area is easily identifiable due to the lack of hair follicles and sweat glands,

which under H&E staining is seen in dark blue or purple areas. In addition, there seems to be an increase of subcutaneous tissue under the wounded area in the *Ext1*$^{+/-}$*Ext2*$^{+/-}$ subjects.

Greater magnification of the wound areas identified previously were further investigated. Two different types of histology staining were used to show cell proliferation is increase in the *Ext1*$^{+/-}$*Ext2*$^{+/-}$ subjects compared to the control of the dorsal cutaneous wounds at 14 days post wounding (**Figure 1.5**). H&E staining is commonly used because the hematoxylin stains cell nuclei blue and eosin stains the extracellular matrix and cytoplasm pink. In addition, an antibody Ki67 was used to target the DNA within cells, specifically the surface of mitotic chromosomes in the perichromosomal layer which stain brown in the images. H&E staining and Ki67 antibody were used to quantify cell proliferation in the wounded areas, such that there appears to be more cell nuclei present in the *Ext1*$^{+/-}$*Ext2*$^{+/-}$ mice. Panel A represents the wildtype skin and a greater magnification of the dotted box, the magnification bars are given. This data indicates that there is an increase in cell proliferation in the *Ext1*$^{+/-}$*Ext2*$^{+/-}$ subjects. Thus, the enhanced rate of wound closure in *Ext1*$^{+/-}$*Ext2*$^{+/-}$ reflects an increase in cell proliferation in the wound area.

Based on these results, the next objective of this project was to determine the quantity of heparan sulfate and chondroitin sulfate in the dorsal cutaneous tissue. As stated previously, the *Ext1*$^{+/-}$*Ext2*$^{+/-}$ mutation was expected to cause a decline in heparan sulfate levels. Chondroitin sulfate typically increases in cell lines when heparan sulfate is reduced (Zak, et al., 2011). In order to quantify the heparan sulfate and chondroitin sulfate expression, uninjured dorsal cutaneous tissue was collected, digested to disaccharides, and analyzed by liquid chromatography/mass spectrometry. A 15 x 30mm section of tissue was collected from wildtype, *Ext1*$^{+/-}$, *Ext2*$^{+/-}$, and *Ext1*$^{+/-}$*Ext2*$^{+/-}$ mice. The quantification of the various genotypes in micrograms of heparan sulfate per gram of tissue in terms of dry weight was determined (**Figure 1.6**). It was found that the

wildtype dorsal cutaneous tissue had an average of 157.8 ± 44.4μg/g, the *Ext1*$^{+/-}$ tissue had an average of 50.4 ± 35.5μg/g, the *Ext2*$^{+/-}$ tissue had an average of 30.8 ± 8.9μg/g, and the *Ext1*$^{+/-}$ *Ext2*$^{+/-}$ tissue had an average of 48.6 ± 19.1μg/g. Published data indicates that the heparan sulfate expression in mice should be approximately 125 μg/g of tissue, but did not specify the gender or location the skin sample was taken from (Ledin, et al., 2004). Thus, inactivation of *Ext* gene caused a decrease in heparan sulfate *in vivo*.

To examine how altering *Ext* expression affects chondroitin sulfate, the GAG fraction isolated from cutaneous tissue was digested with chondroitinase ABC and the disaccharides were quantitated by LC/MS (**Figure 1.7**). Wildtype dorsal cutaneous tissue had an average of 63.3 ± 1.1μg/g, the *Ext1*$^{+/-}$ tissue had an average of 50.2 ± 1.9μg/g, the *Ext2*$^{+/-}$ tissue had an average of 55.1 ± 5.8μg/g, and the *Ext1*$^{+/-}$*Ext2*$^{+/-}$ tissue had an average of 42.8 ± 2.2μg/g. Thus, no significant decrease or effect in chondroitin sulfate levels with the *Ext1*$^{+/-}$*Ext2*$^{+/-}$ mutation was noted. This is a novel finding and only further provides support that *Ext1*$^{+/-}$*Ext2*$^{+/-}$ mutation only influences heparan sulfate expression *in vivo* in the skin.

DISCUSSION

The double heterozygous *Ext1*$^{+/-}$ *Ext2*$^{+/-}$ has proven to enhance wound healing significantly. The heparan sulfate expression decreased by more than 50%, however the wildtype expression did not match that of previous literature. The literature from 2004 that reported heparan sulfate levels in mouse skin did not report the area of skin extracted, nor did they report the age or gender of the mice used in the experiment (Ledin, et al.). Here we report the heparan sulfate levels found in 8-week-old male C57BL/6 mice from 15mm x 30mm dorsal skin. Although the data appears to be promising, the data were not too accurate across the replicates. Ideally, in the future,

it would be preferred to have another set of three replicates to get a better idea of the heparan sulfate expression in cutaneous tissue.

Furthermore, it would be interesting to manipulate chondroitin sulfate levels through the enzyme chondroitin sulfate synthase 1 (CHSY1) which is one of many enzymes that biosynthesizes chondroitin sulfate. If CHSY1 expression is downregulated in fibroblasts, the expression of a cysteine-aspartic acid protease caspase 1 (CASP1) also decreased (Au-Yeung, et al., 2011). CASP1 plays a role in both cell proliferation and cell migration, thus decreasing the expression would slow the wound healing process. Thus, CHSY1 enzyme expression could be influenced to upregulate CASP1 expression and increase the wound repair time.

ACKNOWLEDGEMENTS

Chapter 1, in part has coauthored and been executed by Anne Phan. Her previous studies have been incorporated into this thesis with her permission and I thank her and others for allowing me to continue their incredible work. The thesis author is the primary author of this chapter.

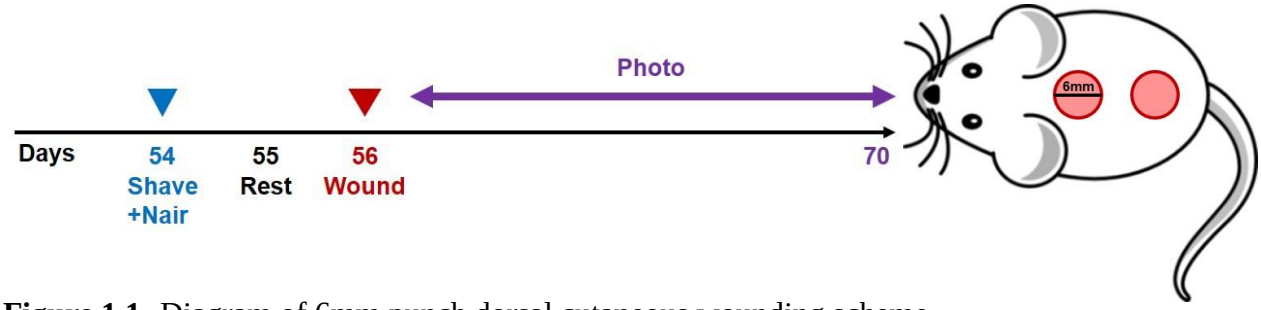

Figure 1.1- Diagram of 6mm punch dorsal cutaneous wounding scheme.

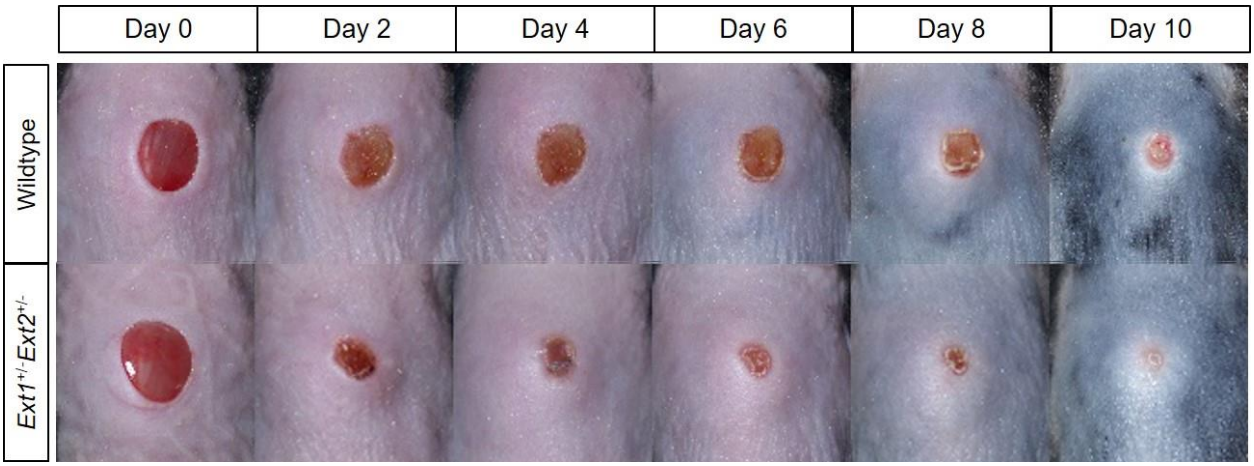

Figure 1.2- Photos of 6mm wounds on live animals; Day 0-10; Wildtype compared to *Ext1*$^{+/-}$ *Ext2*$^{+/-}$.

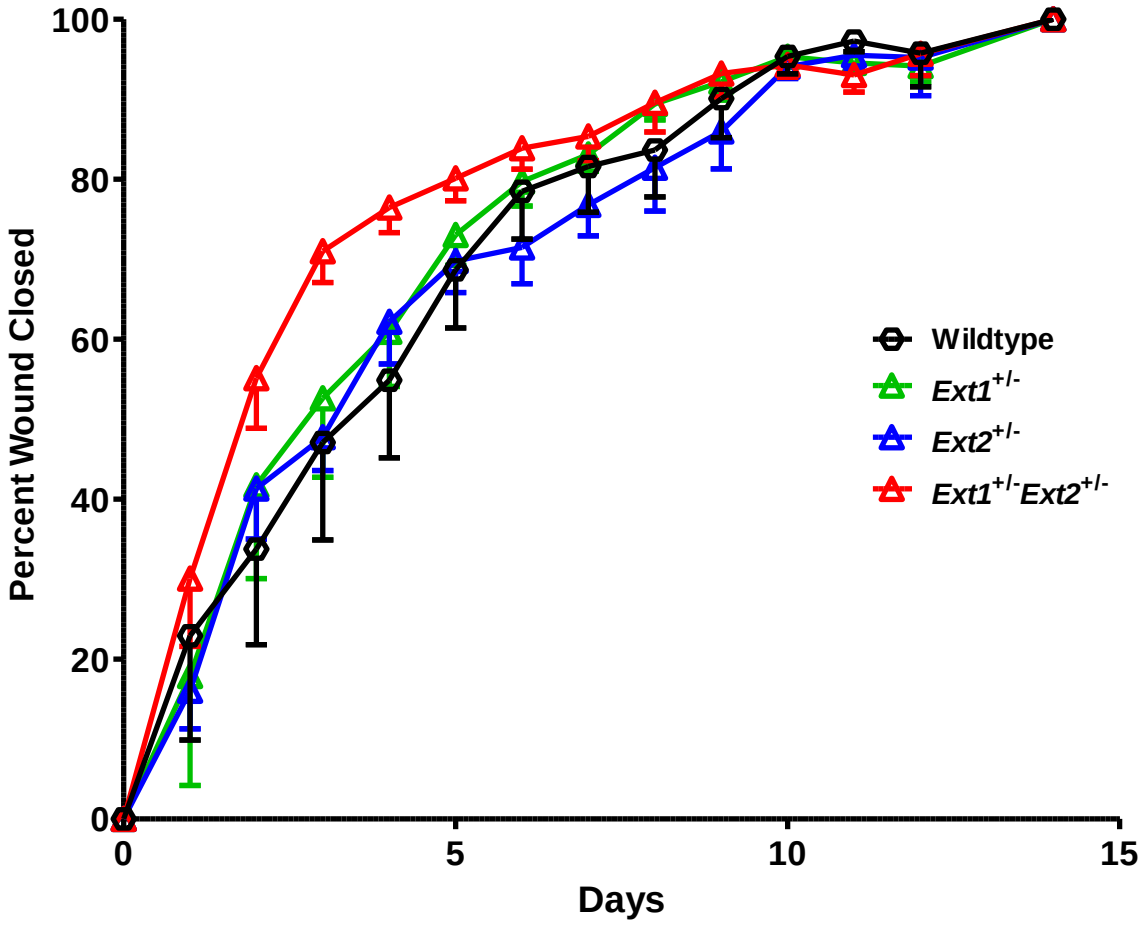

Figure 1.3- Quantification of dorsal cutaneous wound closure over time from the mice in Figure 1.2.

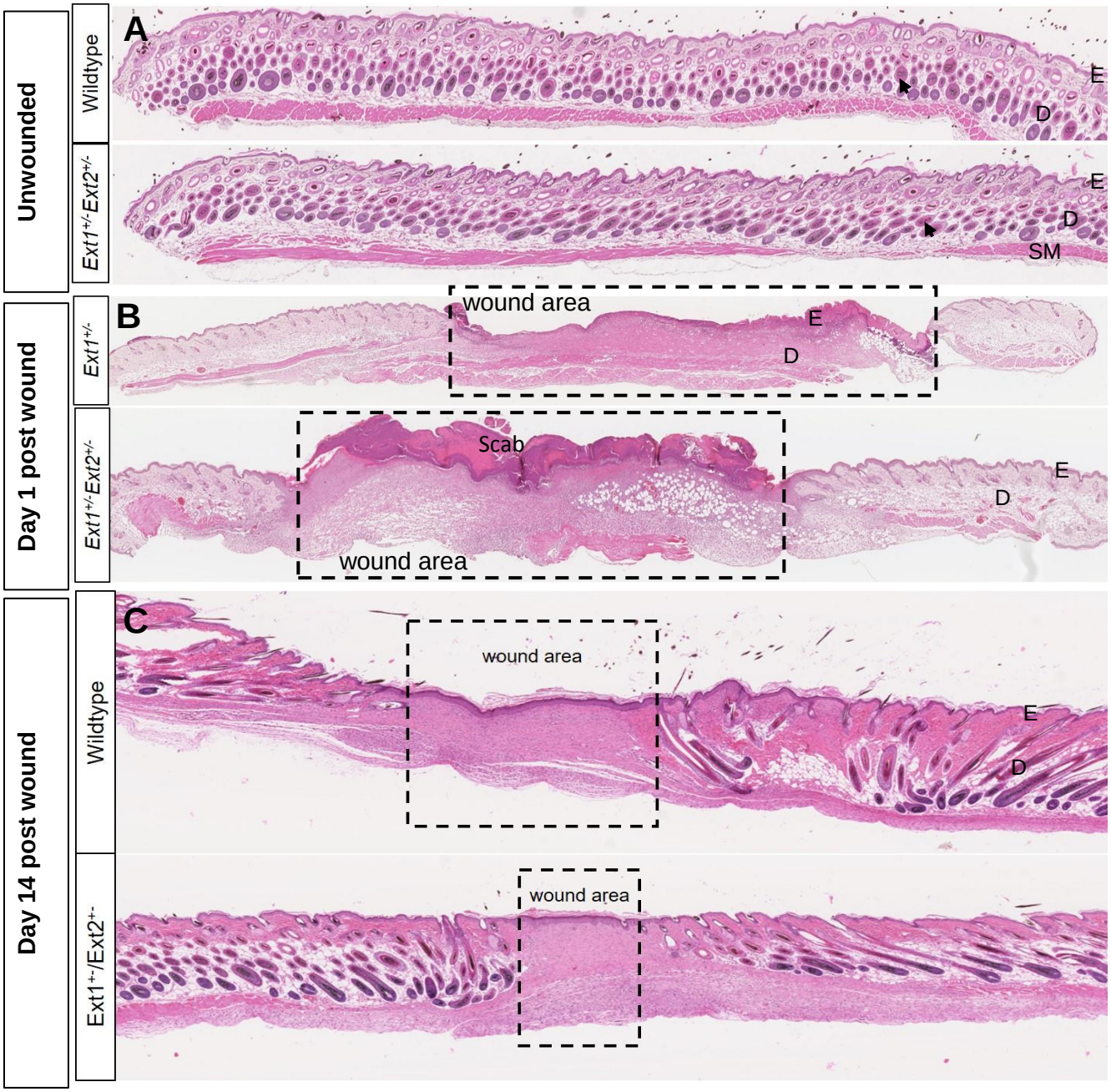

Figure 1.4- Histology of Wildtype and *Ext1*$^{+/-}$*Ext2*$^{+/-}$ wounds; Day 0-12; Staining with Hematoxylin & Eosin.

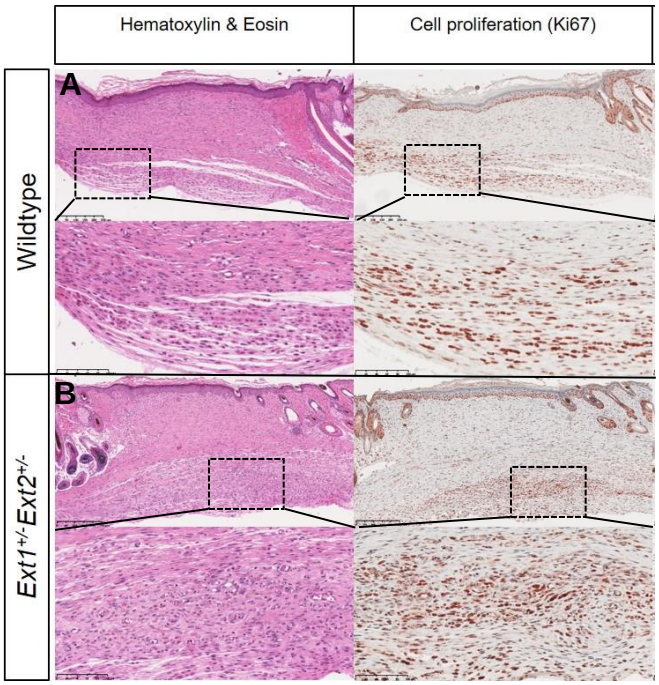

Figure 1.5- Quantification of Figure 1.3. Cell proliferation at Day 14 post-wound shown with Hematoxylin & Eosin and Ki67 staining.

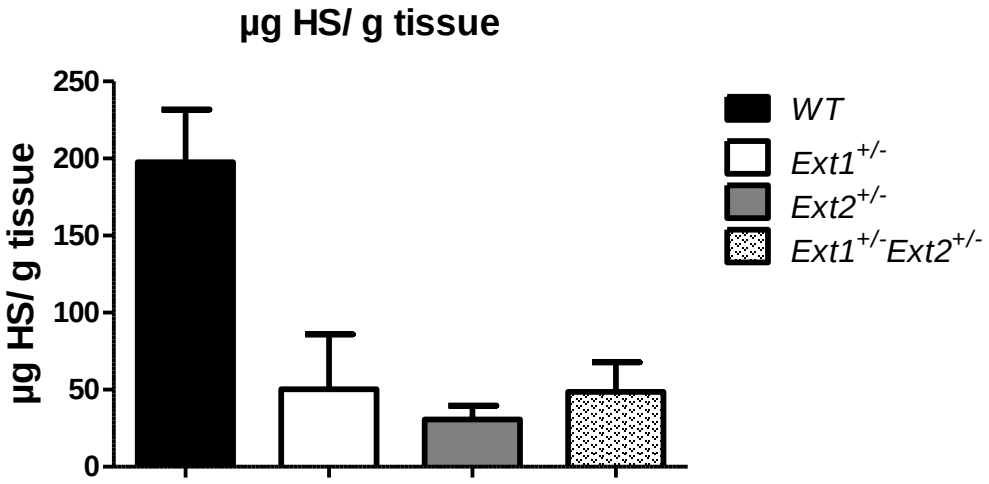

Figure 1.6- Graph of quantification of levels of heparan sulfate in dermal cutaneous wounds (µg of heparan sulfate per gram of dry weight of tissue).

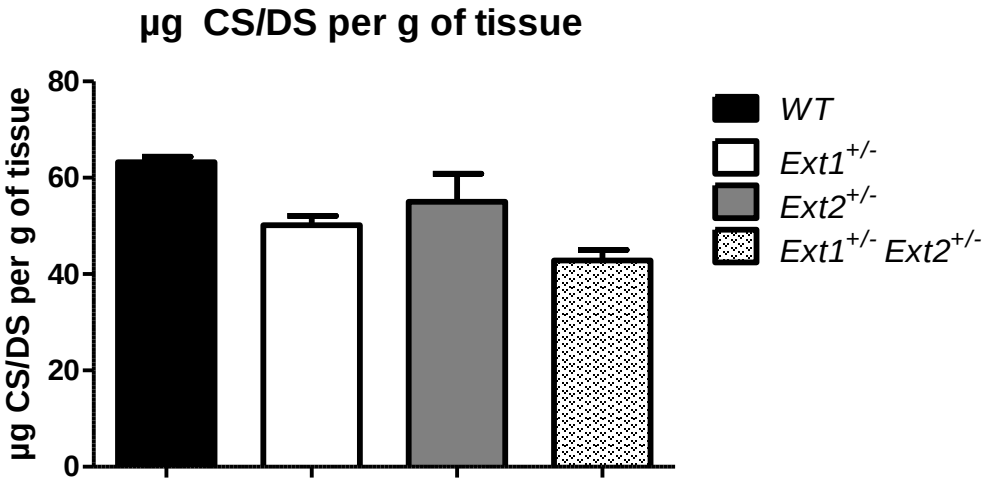

Figure 1.7- Graph of the quantification of levels of chondroitin sulfate/dermatan sulfate in dermal cutaneous wounds (µg of chondroitin sulfate/dermatan sulfate per gram of dry weight of tissue).

Chapter 2

Genetic and Pharmacological Manipulation of Heparan Sulfate Accelerates Cartilage Wound Regeneration

Part I

K14-Cre^{ER}; *Ext1$^{f/f}$*; *mTmG* Mouse Model

INTRODUCTION

The objective of this mouse model was to take a more drastic approach to try and promote wound healing and hopefully regeneration. In this chapter, we will be looking at cartilage wound healing of a through-and-through 2mm diameter ear hole punch. Previously we had attempted to recreate the same mouse model as described in Chapter 1, however there was no change in wound closure in the ears between wildtype, *Ext1*$^{+/-}$, *Ext2*$^{+/-}$, nor *Ext1*$^{+/-}$*Ext2*$^{+/-}$. The transgenic *K14-Cre*^{ER} *Rosa26 mTmG* mice were used the K14 protein promotes the *Cre*-recombinase expression (Squarize, et al., 2010). K14 protein is used in the biosynthesis of epithelia cells and the microfilaments and microtubules in the cytoskeleton (Vasioukhin, et al., 1999; Zimmermann, et al., 2014).

Here we used *K14-Cre*^{ER} *Rosa26 mTmG*, in which the *Cre*^{ER} is a lox tool used on the reported gene to detect a floxed region in the genetic sequence as well as topical tamoxifen to readily depict the genotypes with UV light (Leung, et al., 2015). Under UV light, if the mouse is *Cre*$^{+}$, the green glow indicates that tamoxifen is inducing the recombination of *Ext1*$^{f/f}$ allele, temporarily excising *Ext1*. However, if the mouse is *Cre*$^{-}$, then it will appear red. This is because the reporter system *mTmG* encodes two different phenotypes of fluorescence, *mT* indicates the tomato red color and *mG* indicated the green fluorescent protein in basal keratinocytes (Leung, et al., 2015). *mTmG* is floxed before and after the *mT*, such that when the mouse is *Cre*$^{+}$ the *mT* reporter will be excised and only encode for the green fluorescence protein (GFP) under UV light (Vasioukhin, et al., 1999). Previously, it has been reported that the GFP is localized in the epidermis tissue including hair follicles and sebaceous glands found in the dermis (Leung, et al., 2015). When the wound was inflicted, the GFP remained in the epidermis tissue but was lost from

the dermis and cartilage in the ears, suggesting that the tamoxifen-induced cells most likely contain epithelial stem cells (Leung, et al., 2015).

MATERIALS AND METHODS

Materials. Tamoxifen citrate salt, MP Biomedicals, was used for topical application and purchased from Fisher Scientific (Cat. #ICN15673980). All other materials have been identified in the previous chapter.

Wounding and Imaging. A series of C57BL/6 wildtype mice and genetically modified *K14-Cre^{ER}; Ext1$^{f/f}$; Rosa26 mTmG* mice (all the mice were homozygous for the *Rosa26 mTmG* reporter system) were shaved and treated with Nair to remove all hair from the back of the mice at P52. The mice were then topically treated with Tamoxifen for two days and given a rest day. At P56, the mice were subject to a 2mm ear punch wound in each ear. Each wound on the mice was photographed once a week, for seven weeks, to track the wound closure and healing. In addition, the mice were also imaged using UV light to monitor the expression of *mTmG* based on if the mouse was *Cre*$^{+}$ or *Cre*$^{-}$ once a week. The mice were treated with topical Tamoxifen on a bi-weekly schedule. Wound size quantification was done using ImageJ programming.

Histology. At the end of the wound healing process, the mice were sacrificed. The whole ear of each mouse was collected for histology for each genotype. The ear was then cut down evenly through the wounded area. The ear was embedded in Paraffin such that it would be cut into 5µm sections by a rotary microtome in a sagittal direction in reference to the skin. The samples were then placed on positively charged glass slide and let to dry overnight. The slides were then subject to Hematoxylin & Eosin (H&E) staining as described in Chapter 1 and imaged on the NanoZoomer digital slide scanner.

The slides were then subject to Trichrome staining. The slides were de-paraffinized and rehydrated and then placed in Bouin's solution overnight at room temperature. The slides were washes with running tap water, placed in Weigert's iron hematoxylin solution for 5 minutes, rinsed with running tap water for 5 minutes, rinsed in DI water, placed in Bierbrich Scarlet-Acid Fuchsin solution for 5 minutes, rinsed in DI water, placed in a PMA/PTA solution for 5 minutes, rinsed with DI water, placed in aniline blue for 5 minutes, placed in 1% Glacial acidic acid in MilliQ water for 2 minutes, rinsed with DI water, and dehydrated in xylene. The slides were then covered with 0.5mL of 10µL/mL of anti-aggrecan antibody in 1% BSA for 2 hours at room temperature. Finally, permanent mounting media was used to seal a coverslip to the slide and let dry until imaging.

RESULTS

The results in chapter 1 indicated that reduction of heparan sulfate enhanced dermal wound repair. The primary focus of this chapter was to investigate if these findings could be extended to other tissues, in particular cartilage regeneration. To study this problem, we developed a wound model in which the ear was punched with a 2 mm diameter wound. Initial experiments using $Ext1^{+/-}$ $Ext2^{+/-}$ or single *Ext* mutants did not show enhanced wound repair in cartilage. To more dramatically alter heparan sulfate *Ext1* was inactivated by expressing *K14-*Cre^{ER} in a strain bearing a conditional floxed allele of $Ext1^{f/f}$ and a reporter gene *Rosa26 mTmG*. Mice were shaved at P52 around the ears and excess hair was removed using Nair. On P53 and P54, the mice were all topically treated with a tamoxifen on their ears. On P56 a 2mm diameter through-and-through punch wound was inflicted on the mice's ears and they were photographed weekly (**Figure 2.1**).

The photographs taken every seven days were used to track the wound closure over time (**Figure 2.2**). Under UV light, the green glow indicates that tamoxifen is inducing the

recombination of *Ext1*$^{f/f}$ allele. However, if the mouse is *Cre*$^{-}$, then it will appear red. This is because the reporter system *mTmG* encodes two different phenotypes of fluorescence, *mT* indicates the tomato red color and *mG* indicated the green color. *mTmG* is floxed before and after the *mT*, such that when the mouse is *Cre*$^{+}$ the *mT* reporter will be excised and only encode for the green fluorescence under UV light. The topical tamoxifen is applied biweekly to induce the fluorescence under UV light because the expression fades over time.

Visual inspection of the wounds showed that the tamoxifen induced inactivation of *Ext1*, resulting in more rapid and complete wound closure. The area of wound closure was measured quantitatively by using ImageJ software over a course of seven weeks (**Figure 2.3**). At 14 days post wound, the *Cre*$^{+}$ subjects already show significant cartilage regeneration, closing to approximately 1mm^2. The quantification of wound closure indicates that the average wound area of the *Cre*$^{-}$ mice never close to the same degree as the *Cre*$^{+}$ mice. 21 days post wound shows the greatest wound closure. This is the point at which there is the maximum wound closure, and as healing occurs there is inflammation of the tissue up until the maximum cartilage regeneration. Therefore, the wound area slightly increases after 21 days because there is less swelling at the site of the wound. By the end of the experiment, the *K14-Cre*$^{+}$ *Ext1*$^{f/f}$ *mTmG* mice had an average wound area of 1.5 ± 0.61mm^2, and the *K14-Cre*$^{-}$ *Ext1*$^{f/f}$ *mTmG* had an average of 2.6 ± 0.40mm^2. That resulted in 53% wound healing to a 23% wound healing, respectively. The mice were imaged until 96 days post wound, however there was little to no change after 49 days post wounding. The 2mm ear punch wound never healed or closed completely however. Overall, there was a significant effect in cartilage regeneration in the *K14-Cre*^{ER} *Ext1*$^{f/f}$ *mTmG* mouse model.

In order to track the wound regeneration on a cellular level, the ears of the mice were collected and embedded in paraffin for sectioning. The ears were first cut down the middle of the

wound from the tip of the ear to the base and then the wounded edges of the ear were mounted in paraffin vertically wound side down (**Figure 2.4**). Once the sections were made, the tissue was stained with trichrome staining. The primary area of interest was the edges of the wound that regenerated and healed.

Under greater magnification the cell growth could be identified. Towards the center of the tissue section, in both models, there are white circles, or spaces, which is consistent with cartilage histology, labeled as "C". The epidermis and dermis were also identified and labeled as "E" and "D", correspondingly. In the red dotted area of the *K14-Cre^{ER} Ext1$^{f/f}$* tissue, indicates the growth of new cartilage. The new cartilage begins to form at the arrow head and the chondrocytes were located and labeled "Ch". This is so the newly developed cartilage can grow and form with the existing cartilage. In the *Ext1$^{f/f}$* tissue, there is little to none new cartilage being formed, and no chondrocytes were identified. This data is consistent with the increased wound healing in the *K14-Cre^{ER} Ext1$^{f/f}$ mTmG* mice.

The *Ext1$^{f/f}$* tissue shows a thinner perichondrium, labeled "P", shown in the black box, as compared to the *K14-Cre^{ER} Ext1$^{f/f}$* tissue, as seen as the pink tissue layer at the site of the wound. The perichondrium is the layer of connective tissue that surrounds the cartilage in the ear. It appears pink under trichrome staining because the perichondrium layer consists of fibroblasts, which synthesizes extracellular matrices. The perichondrium also functions in repairing cartilage, which would explain why the *K14-Cre^{ER} Ext1$^{f/f}$* tissue has a thicker layer of perichondrium because there was greater wound regeneration in that mouse model. These findings are consistent with other literature, as there is greater blastema formation, the perichondrium thickens and reduces scarring (Metcalfe, et al., 2006).

DISCUSSION

K14-Cre^{+} *Ext1*$^{f/f}$ mice showed significant wound repair compared to the *K14-Cre*$^{-}$ *Ext1*$^{f/f}$ mice, resulting in 53.4% wound healing to a 22.7% wound healing, respectively, after 49 days. Not only did the *K14-Cre*$^{+}$ *Ext1*$^{f/f}$ mice have an accelerated repair rate, but there were also the beginning stages of regeneration. Newly formed chondrocytes were identified in the wounded tissue as well as thickening of the perichondrium. Since, K14 protein is used in the biosynthesis of epithelia cells and the microfilaments and microtubules in the cytoskeleton, we believe the *K14-Cre*$^{+}$ *Ext1*$^{f/f}$ mice healed faster because of the location of the wound. Ears have a thin layer of cartilage throughout and epithelial cells making up the epidermis and dermis on either side of the cartilage. The *K14-Cre*$^{+}$ *Ext1*$^{f/f}$ mouse model took a dramatic approach to achieve wound regeneration by including a knockdown of heparan sulfate, through the temporary excision of *Ext1*$^{f/f}$, and a *K14* promoter resulting in increased K14 protein and consequently promoting epithelial cell production. To further these findings, the next steps would be to observe the GFP with immunohistochemistry. This would allow us to determine which specific cells are involved in the regeneration and repair. Overall, this *K14-Cre*$^{+}$ *Ext1*$^{f/f}$ genetic manipulation had novel findings and proves that regeneration can be achieved in mice.

ACKNOWLEDGEMENTS

Chapter 2, in part has coauthored and been executed by Anne Phan. Her previous studies have been incorporated into this thesis with her permission and I thank her and others for allowing me to continue their incredible work. The thesis author is the primary author of this chapter.

Figure 2.1- Diagram of 2mm ear punch wounding scheme in *K14 Cre^{ER} Ext1$^{f/f}$ Rosa26 mTmG*.

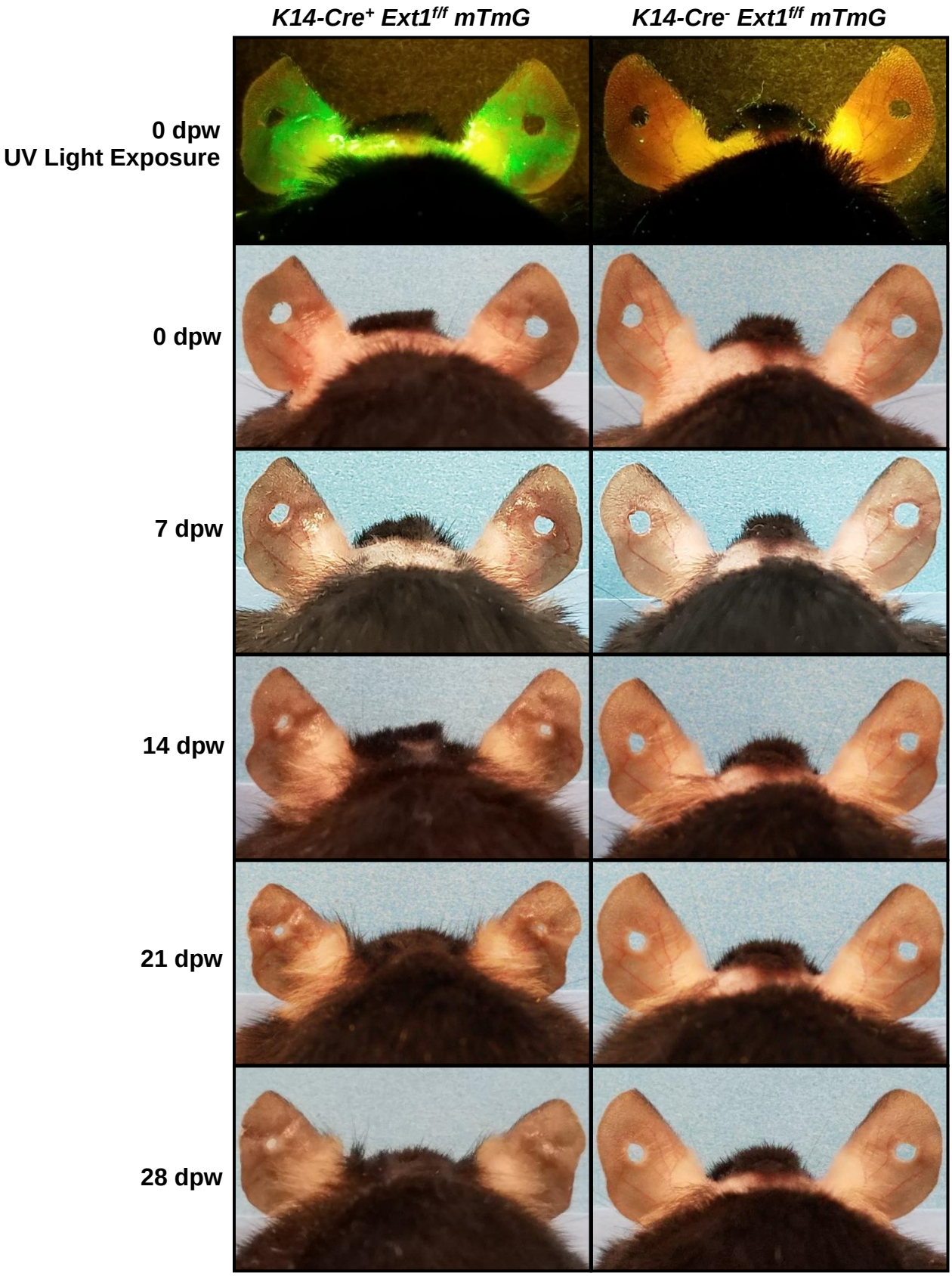

Figure 2.2- Photos of 2mm ear wounds on live animals; Day 0-25; *K14-Cre^{+} Ext1$^{f/f}$ mTmG* compared to *K14-Cre^{-} Ext1$^{f/f}$ mTmG*.

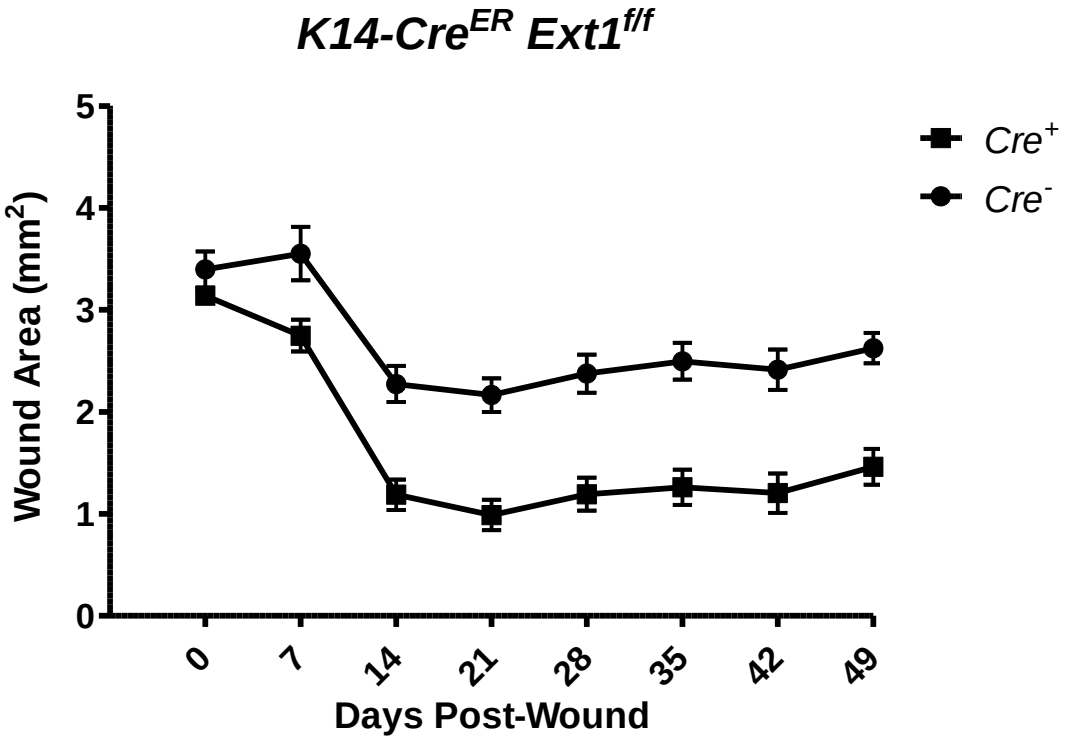

Figure 2.3- Graph of the quantification of 2mm ear wound closure; Day 0-49.

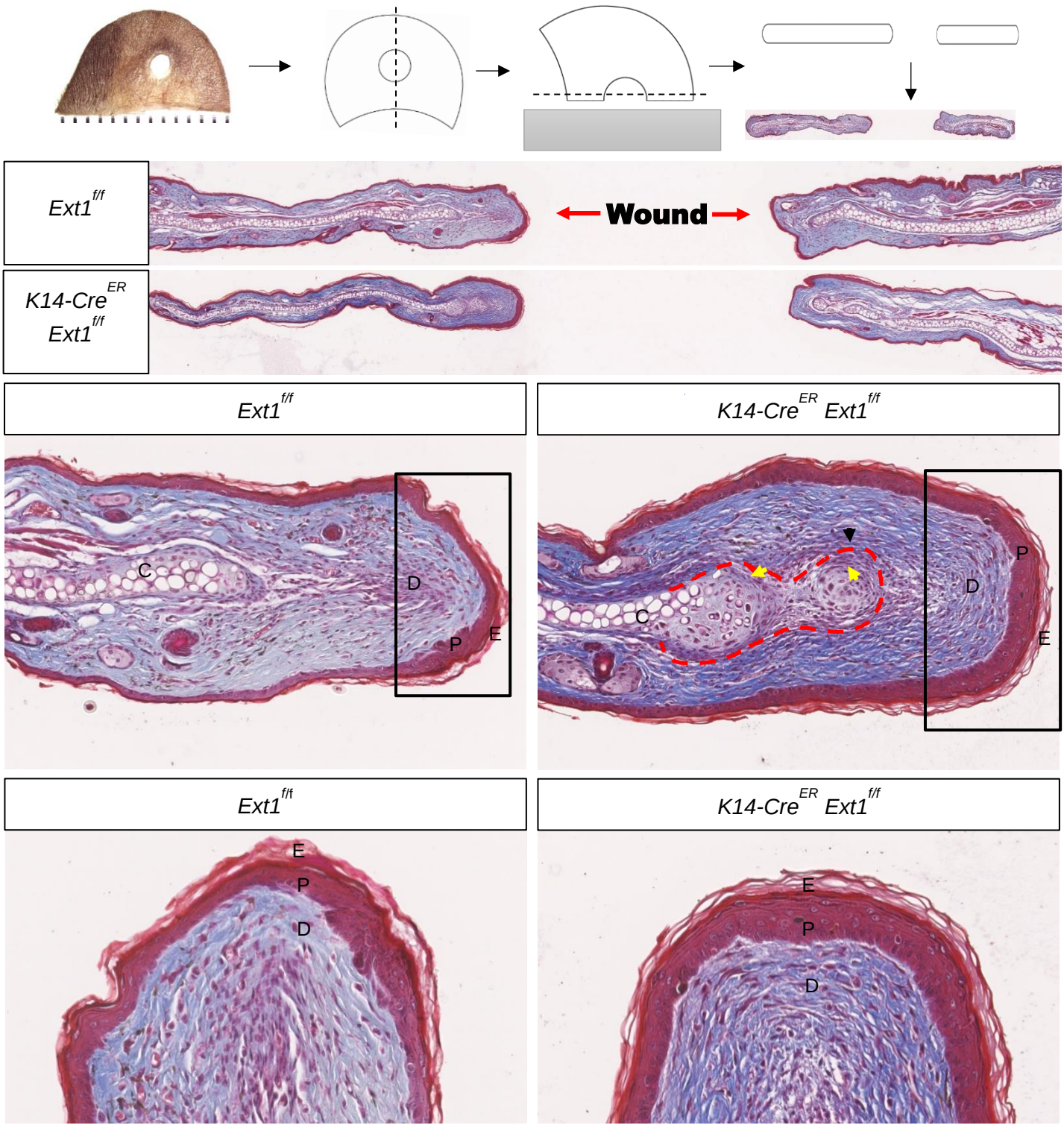

Figure 2.4- Histology of *K14-Cre*$^{-}$ *Ext1*$^{f/f}$ and *K14-Cre*$^{+}$ *Ext1*$^{f/f}$ 2mm ear punch wound closure with trichrome staining. "D" dermis; "E" epidermis; "P" perichondrium; "C" cartilage; yellow arrow heads indicate chondrocytes; red outline indicates new growth.

Part II

Xyloside Mouse Model

INTRODUCTION

To further the investigation on the manipulation of heparan sulfate and its effects on wound healing, we set out to create a different mouse model that could do just that. When synthesizing proteoglycans, glycosaminoglycans become linked to a tetrasaccharide β-linked to a serine residue on the core protein (Fritz, et al., 1997; Varki, et al., 2017). The tetrasaccharide consists of GlcAβ1→3Galβ1→3Galβ1→4Xylβ1-Serine, and depending on the glycosaminoglycan that is being synthesized, either β-GalNAc or α-GlcNAc is initially added to the reducing end of the tetrasaccharide (Fritz, et al., 1997; Varki, et al., 2017). Since a xyloside is the bridge between the forming glycosaminoglycan chain and the core protein, it has also been found that xylosides can act as an alternate substrate for the synthesis of the glycosaminoglycans (Lugemwa and Esko 1991; Miao, et al., 1995; Fritz and Esko, 2001)

Here we describe how a synthetic xyloside was made to decrease the levels of heparan sulfate found at the cell surface, essentially, inhibiting the biosynthesis of glycosaminoglycans. The study of how different xylosides affect the synthesis and priming of chondroitin sulfate and heparan sulfate has been around for decades. The most notably β-D-xyloside has been found to prime and synthesize mainly chondroitin sulfate and conservatively heparan sulfate, resulting in the synthesis of these glycosaminoglycans to exogenous xyloside primers (Fritz, et al., 1997; Fritz and Esko, 2001). Previously, estradiol β-D-xyloside, in low concentrations, has been reported to inhibit the biosynthesis of heparan sulfate on core proteins on the cell surface (Lugemwa and Esko, 1991).

Most xylosides inhibit the biosynthesis of chondroitin sulfate proteoglycans, however, since we have proven previously in this thesis, the knockdown if heparan sulfate enhances wound healing (Fritz, et al., 1997). Stephen Verespy and Bryce Timm synthesized the xyloside known as

NMX, (2R,3R,4S,5R)-2-(naphthalen-2-ylmethoxy) tetrahydro-2H-pyran-3,4,5-triol, in an effort to decrease the expression of heparan sulfate at the cell surface and enhance wound healing. In addition, a negative control was synthesized to prove NMX is solely an inhibitor of heparan sulfate proteoglycans; this negative control is known as NMA, (2R,3R,4S,5S)-2-(naphthalen-2-ylmethoxy) tetrahydro-2H-pyran-3,4,5-triol). The goal is to determine if the C57BL/6 mice that are given a through-and-through 2mm diameter ear hole punch have an enhanced wound repair when given 1mM NMX drinking source *ad libitum*.

MATERIALS AND METHODS

Materials. Bouin's solution was bought from Ricca Chemical (Cat. #1120-32). Weigert's iron hematoxylin solution A and B was bought from Harleco (Cat. #15204-220, #15204-222). Bierbrich Scarlet-Acid Fuchsin solution, Phosphotungstic Acid solution (PTA), Phosphomolybdic acid solution (PMA), and Aniline Blue Solution was bought from Sigma (Cat. #HT15-1, #HT15-2, #HT15-3, #HT15-4). Glacial acidic acid was bought from Fisher Scientific (Cat. #A38-500). Anti-Aggrecan antibody was bought from Millipore Sigma (Cat. #AB1031).

Compound Synthesis. Synthesis of NMX1 ((3R,4S,5R)-tetrahydro-2H-pyran-2,3,4,5-tetrayl tetrabenzoate): An anomeric mixture of $_{D}$-(+)-xylose (10g, 66.61mmol) was added to a 500mL round bottom flask with a stir bar and to this was added 816mg of DMAP (0.1 eq., 6.661mmol) The flask was then purged with nitrogen and 100mL of dry pyridine was cannulated into the flask and a nitrogen balloon was fixed to the flask. The solution was then immersed in an ice bath (0^{o}C) and 46mL of BzCl (6 eq., 400mmol) was added slowly to the stirred solution over the course of 0.5h. The reaction was then allowed to slowly come to room temperature and remained for a total of 24h. Upon completion, 150mL of DCM and 100mL of 2N HCl (aq.) was added to the flask and the solution was transferred to a 500mL separatory funnel. The organic layer was then washed 2x

with 2N HCl and subsequently, once with saturated NaCl (aq.) solution (brine). The organic layer was then washed 2x with sat. $NaHCO_3$ (aq.) solution and once with brine. The organic layer was dried over $MgSO_4$, filtered into a 500mL round bottom flask and condensed under vacuum to give an off-white/pale yellow thick oil, that upon standing gave way to NMX1 a waxy semisolid (34g, 90%) without further purification.

Synthesis of NMX2 ((3R,4S,5R)-2-hydroxytetrahydro-2H-pyran-3,4,5-triyl tribenzoate): In a 250mL round-bottom flask, 14g of NMX1 (24.7mmol) was added, charged with a stir bar, and suspended in 75mL of dry DCM. The solution was placed in an ice bath and to this was added 36mL of 33% w/w HBr/AcOH (8 eq., 197.7mmol). The resulting solution turned yellow and after 1.5h at 0 ^oC, an additional 50mL of DCM was added to dilute and was then quenched with 100mL of sat. $NaHCO_3$ (aq.) solution. The biphasic solution was transferred to a separatory funnel and the organic layer was washed 3x with additional 200mL of $NaHCO_3$ (aq.) (until gas was no longer released) and once with 100mL of brine. The organic layer was separated, dried over $MgSO_4$, and filtered into a clean, dry 500mL round-bottom flask and condensed to a clear, pale yellow oil/semisolid. The resulting intermediate was immediately dissolved in 5:1 acetone: water (60mL) and stirred at room temperature. To the stirred solution, 7.3g of Ag_2CO_3 (1.5 eq., 26.48mmol) was added and stirred vigorously for 1.5h. Upon completion, the solution was filtered through a pad of celite and the volatiles were removed under vacuum. The white residue was then diluted with 150mL of EtOAc and 100mL of water and transferred to a separatory funnel. The organic layer was washed 2x with water, once with brine, and dried over Na_2SO_4. The resulting solution was filtered into a 250mL round-bottom condensed under vacuum to afford an off-white semisolid. DCM was then added to solubilize the residue and to this silica gel was added to the solution to create a slurry for dry loading. The slurry was condensed to dryness under vacuum and the loaded

silica was placed over a short pad of silica in a column and covered with sand. 300mL of 12% EtOAc in hexanes was flowed through the silica and the starting material was collected. Then 450mL of 40% EtOAc in hexanes was flowed through the silica to obtain the two anomers of product. The solution was condensed under vacuum and placed on high vac to yield a white foam then solid.

Synthesis of NMX3 ((3R,4S,5R)-2-(2,2,2-trichloro-1-iminoethoxy) tetrahydro-2H-pyran-3,4,5-triyl tribenzoate): To the 11g of NMX2 (23.85mmol) in a 250mL round-bottom flask, a stir bar was added, and the semisolid was dissolved in 125mL of dry DCM under nitrogen atmosphere. To this, 9.6mL of CCl_3CN (4 eq., 95.4mmol) was added and the solution was placed in an ice bath and stirred with a nitrogen balloon attached. A catalytic amount of DBU (200µL) was added to the stirred solution and the reaction was allowed to proceed for 18h at 0 ^oC. After the allotted time, DCM was used to wash the stir bar and dilute the reaction mixture. The volatile components were then removed under vacuum and the condensed oil was dissolved in 20% EtOAc in hexanes. The dissolved solution was then passed through a silica plug and washed 50mL of 20% EtOAc in hexanes 3x. The collected solution was condensed under vacuum to give a yellow viscous oil and was placed under high vac to afford a pale-yellow solid as NMX3 (13.35g, 92%).

Synthesis of NMX4 ((2R,3R,4S,5R)-2-(naphthalen-2-ylmethoxy) tetrahydro-2H-pyran-3,4,5-triyl tribenzoate): The flask containing NMX3 (13.35 g, 22.04mmol) was equipped with a stir bar, placed under vacuum, and the atmosphere was replaced with nitrogen. 2-naphthalenemethanol (5.23g, 1.5 eq., 33.065mmol) was added to the flask, as well as 5g of activated 4Å molecular sieves. The flask was again pumped under vacuum and the atmosphere was replaced with nitrogen and capped with a rubber septum. DCM (110mL) was cannulated into the flask and the solution was placed in chilled bath (0 ^oC) fixed with a nitrogen balloon. After

stirring for 10 minutes, 400 µL of TMSOTf (0.1 eq. 2.204mmol) was added dropwise to the solution through the septum. The reaction continued at 0 ^{o}C for 18h and was then quenched by adding 600mg of $NaHCO_3$ (s) (0.3 eq., 6.613mmol) directly to the solution and stirred for 15 minutes. The contents of the flask were then filtered through a pad of celite, washed with DCM, and condensed under vacuum to produce a yellow viscous oil. For small scale purification to obtain an analytically pure sample, the product can be isolated by normal phase column chromatography (NMX4 R_f = 0.35 in 30% EtOAc in hexanes). Otherwise, the crude oil is dissolved in 20% EtOAc in hexanes and passed through a 50 g silica plug. Subsequently, 200mL of 40% EtOAc in hexanes was passed through the plug, collected, and condensed under vacuum. The crude material was then carried forward to the next reaction.

Synthesis of NMX ((2R,3R,4S,5R)-2-(naphthalen-2-ylmethoxy) tetrahydro-2H-pyran-3,4,5-triol): The flask containing the crude material of NMX4 (18g) was equipped with a stir bar and dissolved in 40mL of dry DCM. To this, 120mL of dry methanol was added to the solution and placed under nitrogen atmosphere at room temperature. After stirring for 10 minutes, a catalytic amount (150µL) of a 5.4M CH_3ONa solution was added to the stirred solution. After reacting for 4h and monitoring consumption of starting material by TLC, Dowex 50WX8 (H^+) was added to quench the CH_3ONa and allowed to continue stirring for 10 minutes. The solution was then filtered into a 250mL round bottom flask to remove the Dowex and the solution was concentrated under vacuum to produce an orange/yellow residue. 100mL of HPLC grade EtOAc was added to the flask and heated to dissolve the residue and allowed to recrystallize. The recrystallization afforded small off-white/tan needles. This was filtered, washed with cold EtOAc, the crystals collected, and the eluent was condensed. The recrystallization was performed again, and the crystals produced were filtered out and combined with the previous batch. The collected

crystals were then dissolved in hot water and allowed to recrystallize again, producing long white/colorless needles. The crystals were then filtered, washed with water, collected, and lyophilized to remove any excess water (5.88g, 92%).

Synthesis of NMA ((2R,3R,4S,5S)-2-(naphthalen-2-ylmethoxy) tetrahydro-2H-pyran-3,4,5-triol) was performed using the same procedures as for NMX (29% overall yield).

Wounding and Imaging. A series of C57BL/6 wildtype mice were shaved and treated with Nair to remove all hair from the back of the mice at P54. At P56, the mice were subject to two 6mm, in diameter, dorsal cutaneous punch wounds. Each wound on the mice was photographed everyday over a course of 14 days to track the wound closure and healing.

A cohort of C57BL/6 wildtype mice were introduced to designated drinking source *ad libitum* at P44. The mice were allowed their normal diet and only allotted the given drinking source of either water, NMA, or NMX. At P65, the mice were subject to a 2mm ear punch wound in each ear. Each wound on the mice was photographed once a week, for seven weeks, to track the wound closure and healing. Wound size quantification was done using ImageJ programming.

RESULTS

This portion of the project to investigate cartilage regeneration was dependent on the synthesis of NMX ((2R,3R,4S,5R)-2-(naphthalen-2-ylmethoxy) tetrahydro-2H-pyran-3,4,5-triol) and NMA ((2R,3R,4S,5S)-2-(naphthalen-2-ylmethoxy) tetrahydro-2H-pyran-3,4,5-triol). The synthesis of scheme of NMX, and NMA was synthesized similarly is represented in a flow diagram (**Figure 3.1**). The synthesis of NMX and NMA were performed entirely by Steven Verespy and Bryce Timm of the Kamil Godula lab. The overall yield of NMX was 59% and NMA overall yield was 29%. The solid NMX and NMA were then diluted in water to a concentration of 1mM.

To test if xyloside would enhance wound repair the mice received two 6-mm diameter dorsal cutaneous punch biopsies similar to that of chapter 1. The mice were imaged on the day of wounding and for two weeks following the punch biopsy and some of the wildtype mice were orally given 1mM NMX *ad libitum*. There was a significant increase in the rate of wound closure as compared to the control wildtype C57BL/6 mice not given NMX beginning after only two days post wounding (**Figure 3.2**). By day four post wound, the xyloside wounds began to scab and almost completely healed by day ten post wound, whereas the wildtype control lagged significantly.

In this mouse model, a cohort of C57BL/6 wildtype mice were used. The independent factor was that the mice were introduced to drinking source *ad libitum* at P44, such that the mice were either only given water, NMA solution, or NMX solution. The mice were then subject to a 2mm ear punch wound at P65 and photographed every seven days for seven weeks (**Figure 3.3** & **Figure 3.4**).

The area of the of the wound was quantified using ImageJ software and graphed (**Figure 3.5**). For the mice given water, NMA, and NMX, the 2mm ear wounds healed quickly by fourteen days post wound. The wound size decreased by 51.5% for mice given water, 52.8% for mice given NMA, and 50.0% for mice given NMX at fourteen days post wound. However, while the wound is healing there is significant inflammation of the tissue surrounding the wound. So, as time goes by and the wound reaches maximum healing, the inflammation decreases resulting in the area of the wound increasing. This trend is observed as the area of the wound increases slightly after twenty-one days post wound. By the end of the experiment, there was no significant difference between the oral supplements on the cartilage regeneration. The mice given water healed 30.3%, the mice given NMA healed 30.0%, and the mice given NMX healed 39.3%. Therefore, the mice

that received NMX did slightly heal better than the controls, however with no significant difference.

DISCUSSION

Often xylosides require an aglycone, which is a compound maintained after the loss of a glycoside and replacement of a hydrogen atom, in order to prime heparan sulfate (Fritz and Esko, 2001). Ideally the aglycones contain one or more fused rings in an attempt to create a more planar configuration. The addition of the two aromatic rings bound to the xyloside in NMX is believed to allow for more efficient priming of heparan sulfate, as previous literature had suggested (Lugemwa and Esko, 1991).

Although the NMX enhanced wound healing significantly in 6mm diameter dorsal wounds, it was not well translated to the wound healing of the cartilage in the ear. This could be for a number of reasons, however NMX still has promising effects on wound healing. Some alternative approaches would be to adjust the concentration of NMX in the drinking source, or even developing a topical treatment with the NMX and NMA. It would be interesting to further the findings from the dorsal wound results and eventually make it applicable to other types of wounding on mammals.

ACKNOWLEDGEMENTS

Chapter 2, part II, in part is coauthored and has been executed by Bryce Timm and Steven Verespy from the Godula lab. Without their work, this mouse model would not have been possible. The thesis author is the primary author of this chapter.

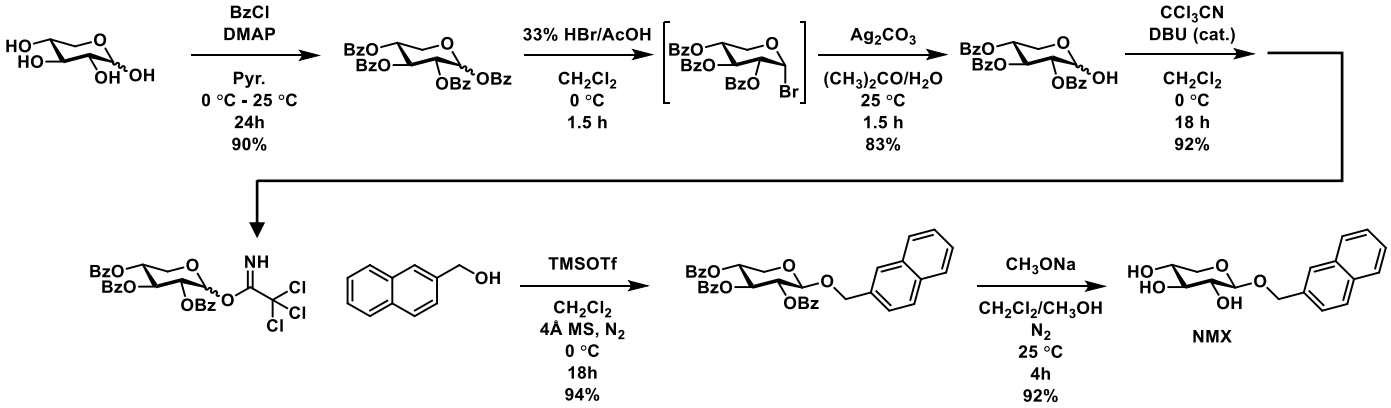

Figure 3.1- Scheme of NMX synthesis.

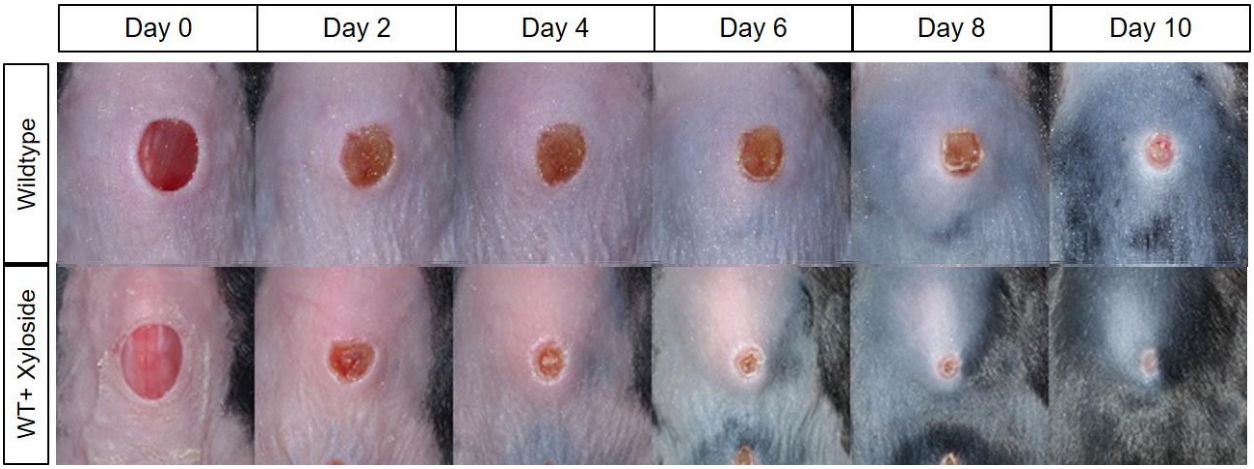

Figure 3.2- Photos of 6mm wounds on live animals; Day 0-10; Wildtype compared to wildtype given 1mM of NMX *ad libitum* as a drinking source.

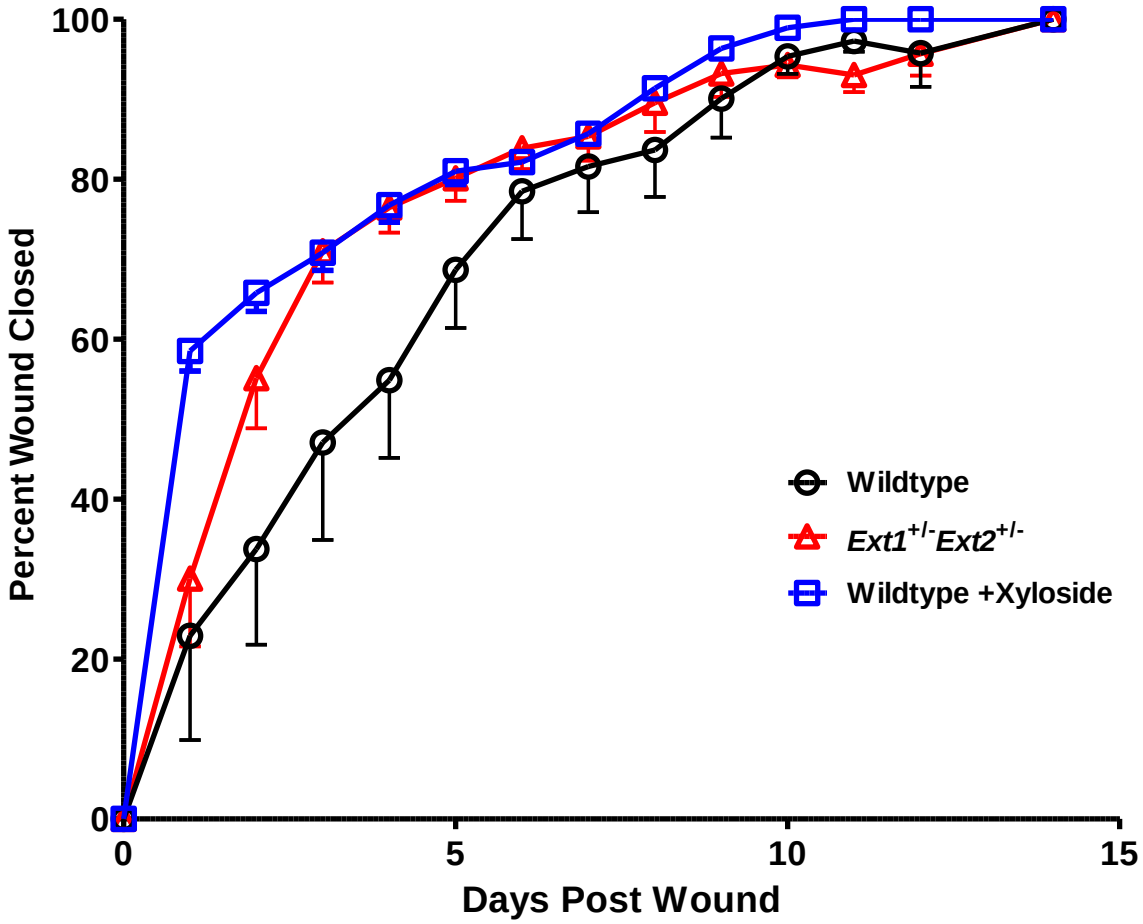

Figure 3.3- Quantification of dorsal cutaneous wound closure over time from the mice in Figure 3.2.

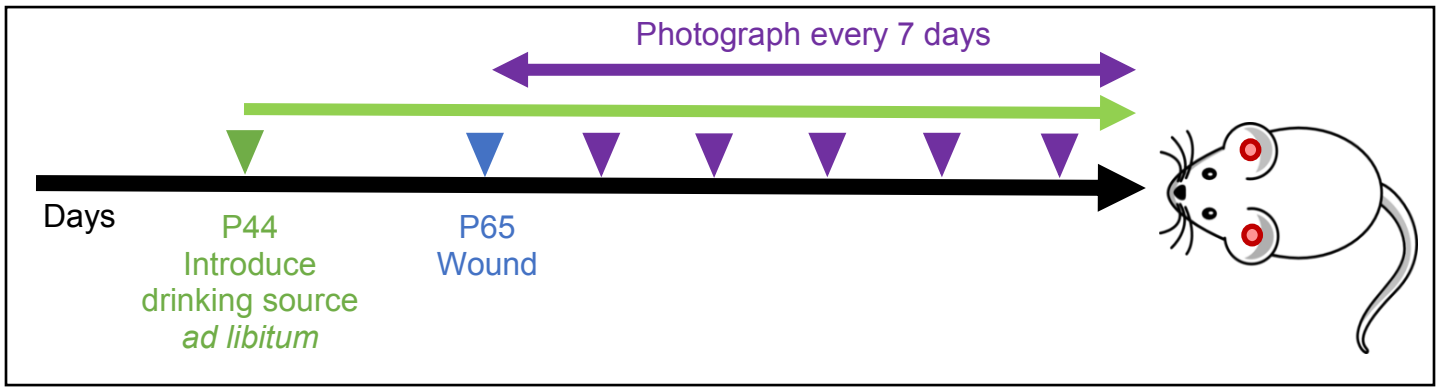

Figure 3.4- Diagram of 2mm ear punch wounding scheme in wildtype mouse model.

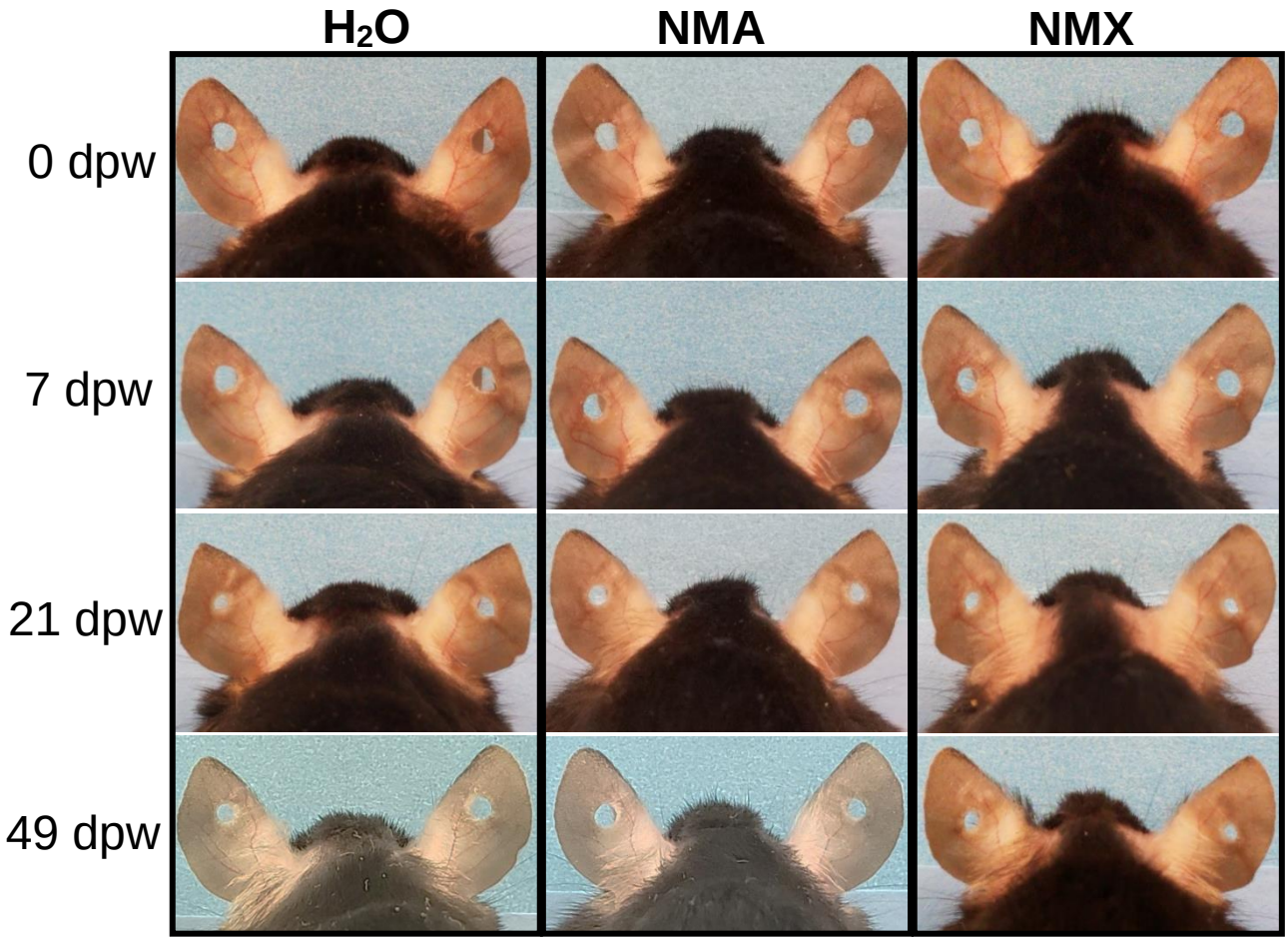

Figure 3.5- Photos of 2mm ear wounds on live wildtype animals *ad libitum* orally given water, NMA, or NMX; Day 0-49.

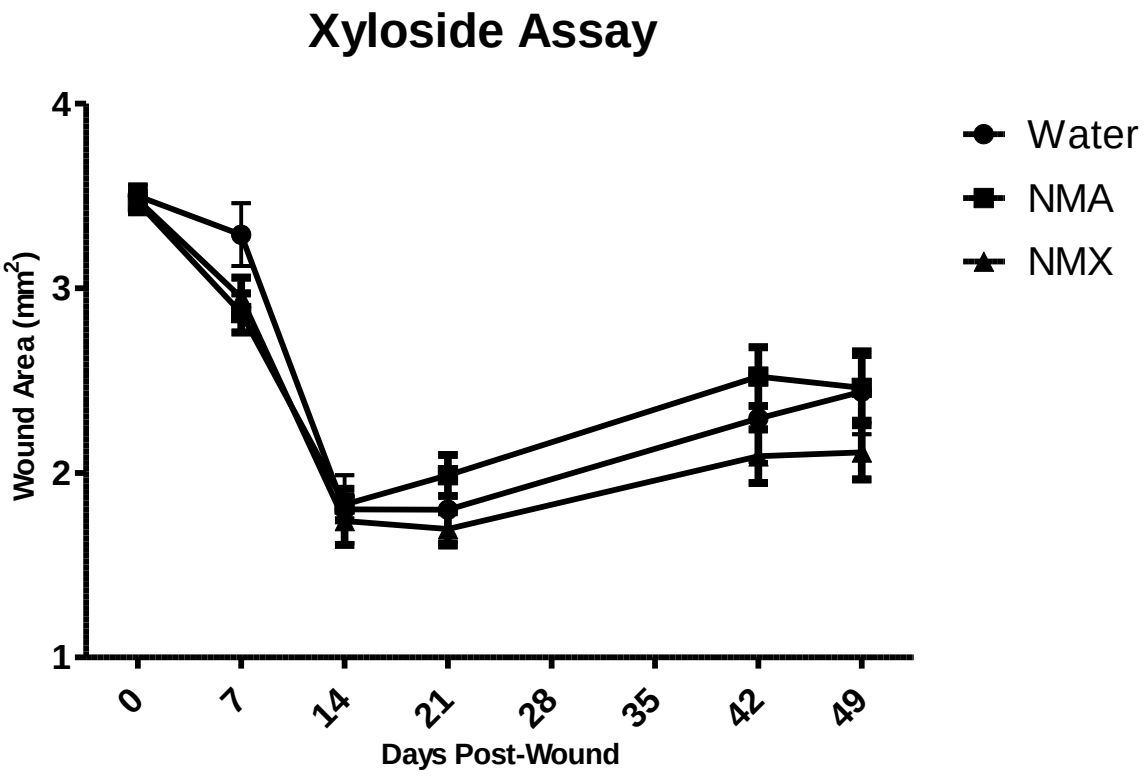

Figure 3.6- Graph of the quantification of 2mm ear wound closure of wildtype mice *ad libitum* orally treated with water, NMA, or NMX; Day 0-49.

Part III

Prrx-Cre^{ER} Ext1$^{+/-}$Ext2$^{+/-}$ Luc$^{/Luc}$ Mouse Model

INTRODUCTION

The *Prrx-1* gene (referred to *Prrx* in this thesis) is first expressed in the mesoderm during the development of an embryo because it plays a key role in cell differentiation (Kern, et al., 1992). *Prrx* is a blastema mesenchymal marker gene, meaning the transcribed protein is expressed in masses of mesenchymal cells, also known as blastema, that are undifferentiated cells that have the capability to develop into other cells as needed for regeneration of a limb or wound (Vogg, et al., 2016). The gene encodes for the protein, paired related homeobox 1, primarily found in cell nuclei. The FGF signaling pathway is known to maintain *Prrx* expression in these blastema (Satoh, et al., 2011). The protein functions as a transcription coactivator, which causes it to bind to an activator to accelerate transcription (Lv, et al., 2016). Zhi-Dong Lv stated in 2016 that when *Prrx* is knocked down, it results in suppression of cellular proliferation and cell migration. In addition, many studies using *ambystoma mexicanumi*, or an axolotl salamander, have shown *Prrx* expression increased significantly in blastema compared to the control intact skin (Sotah, et al., 2010; 2011). Therefore, many sources support that *Prrx* plays a critical role in regeneration, and thus the aim for the *Prrx-Cre^{ER} Rosa26-LSL-Luc* reporter system in this thesis is to determine if *Prrx* is expressed at the site of a wound as it heals.

Once other literature showed a significant phenotype with the *Prrx* gene in regeneration, the next obstacle was to obtain *Prrx-Cre^{ER}* mice and genetically modify them in order to track where *Prrx* is concentrated *in vivo*. A *Prrx-Cre^{ER}-GFP* transgenic mouse model was developed previously and repeated in the laboratory such that it can be induced by tamoxifen for the *Cre* recombinase (Kawanami, et al., 2009). The first impediment to address is that the *Prrx* and *Cre^{ER}* are located in the cytoplasm of the cell; while the *Luc* gene that is responsible for luciferase is located in the nucleus of the cell. *Cre^{ER}* is responsible for cleaving the stop codon that is before

the *Luc* sequence. In order to transport the *Prrx-Cre^{ER}* genes through the nuclear membrane tamoxifen must be present. The tamoxifen is interperitoneally injected into the mice because tamoxifen is not naturally occurring compound in the species. The tamoxifen binds to the *Cre^{ER}* part of the sequence and facilitates the transport, bringing the *Prrx Cre^{ER}* gene sequence into the cell's nucleus. Once in the nucleus, the *Cre^{+}* will induce the cleaving of the stop codon located upstream of the *Luc* gene. The *Rosa26 Luc* genes can then be transcribed to produce the enzyme luciferase (Kawanami, et al., 2009). However, the luciferase enzyme does not have natural luminescence unless paired with the compound luciferin. Luciferin is subcutaneously injected into the mice before *in vivo* imaging with IVIS. The luciferin interacts with the luciferase enzyme resulting in natural luminescence. A visual depiction of the *Prrx-Cre^{ER} Rosa26-LSL-Luc* reporter system is described in **Figure 4.1**. The maximum luminescence occurs fifteen to twenty-five minutes after the subcutaneous injection of luciferin, so the mice were imaged between that time frame.

Prrx-Cre^{ER} Rosa26-LSL-Luc reporter system allows for *in vivo* imaging of the *Prrx*. The aim was to determine if the *Prrx-Cre^{ER} Rosa26-LSL-Luc* mouse model could enhance cartilage regeneration after wounding. The IVIS imaging will be able to determine if the *Prrx* is recruited to the site of the wound, 2mm ear punch wound. If *Prrx* increased limb regeneration in axolotl, the hope is that it will trigger cartilage regeneration in mice. In addition, it will be determined if the *Prrx* gene also accelerates wound regeneration.

MATERIALS AND METHODS

Materials. D-Luciferin Firefly was purchased from Fisher Scientific (Cat. #50853139). Tamoxifen ≥ 99% was used for the intraperitoneal injections and was purchased from Sigma-Aldrich (Cat. #T5648-1G). Anti-Firefly Luciferase antibody was purchased from Abcam (Cat. #ab181640). The

Donkey Anti-Goat IgG Polyclonal Antibody was used as a secondary anti-body and purchased from Neta Scientific (Cat. #LIC-926-32214).

Wounding. A cohort of C57BL/6 mice with various *Prrx Cre^{ER} Rosa26-LSL-Luc Ext1/2$^{+/-}$* genotypes were intraperitoneally injected with Tamoxifen at day P73. The mice were subject to a 2mm ear punch wound in each ear. Each wound on the mice was photographed once a week, for 4 weeks, using the same injections as described previously to track the wound closure and healing. Wound size quantification was done using ImageJ programming.

IVIS Imaging. First the *in vivo* imaging was optimized by taking incremental images to identify at what time point does the luciferase luminescence reached maximum expression. Optimal imaging was determined to be between 15-20 minutes after luciferin injection. At P 80, the mice were subcutaneously injected with Luciferin at time 0 minutes. The mice are then placed in IVIS imaging machine on their left side and imaged 15 minutes after injection for 120 seconds. The mice are then rotated on their right side and imaged 20 minutes after injection for 120 seconds. The mice are then imaged with a camera. Lastly the mice are intraperitoneally injected with Tamoxifen.

Histology. At the end of the wound healing process, the mice were sacrificed. The whole ear of each mouse was collected for histology for each genotype. The ear was then cut down evenly through the wounded area. The ear was embedded in Paraffin such that it would be cut into 5µm sections by a rotary microtome in a sagittal direction in reference to the skin. The samples were then placed on positively charged glass slide and let to dry overnight. Anti-Firefly Luciferase antibody was used to detect luciferase in the tissue. The slides were washed twice in TBS and 0.025% Triton X-100 for 5 minutes with gentle agitation. The slides were then blocked with 1% BSA in TBS for 2 hours at room temperature. The blocker was removed, and the anti-Firefly

Luciferase antibody was applied to the slides in a 1:1000 in TBS with 1% BSA. The slides were once again incubated overnight at 4°C. The slides were washed twice in TBS and 0.025% Triton X-100 for 5 minutes with gentle agitation, then incubated in 0.3% H_2O_2 in TBS for 15 minutes. The secondary antibody, LICOR IRDye 800CW Donkey anti-Goat IgG, was applied to the slides in 1:1000 TBS with 1% BSA and incubated for 1 hour at room temperature. Then they were developed with chromogen for 10 minutes at room temperature. The slides were then rinsed with water and counterstained with hematoxylin. Once the slides were dry, they were cover slipped with mounting media and imaged on the NanoZoomer digital slide scanner. The another set of slides were subject to Trichrome staining as described previously in Chapter 2.

RESULTS

The *Prrx-Cre^{ER} Rosa26-LSL Luc* mouse model experiment was dependent on both luciferin and tamoxifen injections. Luciferin and tamoxifen are compounds that are needed in order to image the luminescence around wound healing as described earlier and in **Figure 4.1**. The tamoxifen binds to the *Cre^{ER}* part of the sequence and facilitates the transport, bringing the *Prrx Cre^{ER}* gene sequence into the cell's nucleus. Once in the nucleus, the *Cre^{+}* will induce the cleaving of the stop codon located upstream of the *Luc* gene. The *Rosa26 Luc* genes can then be transcribed to produce the enzyme luciferase (Kawanami, et al., 2009). Luciferin was subcutaneously injected into the mice before *in vivo* imaging with IVIS. The luciferin interacts with the luciferase enzyme resulting in natural luminescence. The wounding scheme is similar to the previous studies but varies due to the need of tamoxifen and luciferin (**Figure 4.2**). Each cohort of mice were anaesthetized with isoflurane and placed in the IVIS imager. The first set of mice were used to determine the peak in luminescence, and it was found that the luminescence, in photons per second, began at fifteen minutes after the luciferin injection and decreased after thirty minutes.

Each of the genotypes of mice, wildtype, *Ext1*$^{+/-}$, *Cre*$^{+}$ *Luc*$^{/Luc}$, *Cre*$^{+}$ *Ext1*$^{+/-}$ *Luc*$^{/Luc}$, *Cre*$^{+}$ *Ext1*$^{+/-}$ *Ext2*$^{+/-}$ *Luc*$^{/Luc}$, were imaged at approximately fifteen minutes after luciferin injection. The first row shows the mice pre-wound, as a base line of normal luminescence, and the second row shows the expression on day seven post-wound (**Figure 4.3**). All of the images were normalized to be on the same radiance scale. The mice that were *Cre*$^{-}$ do not express any luminescence because the "stop" codon is not excised, and the data were collected supports the genotypes. The hypothesis for the mice that were *Cre*$^{+}$ was that they should have an increased level of radiance expression after wounding at the site of the wound. *Prrx* is known to be expressed in cartilage during production and regeneration, thus the regeneration of cartilage should be able to be tracked and was supported by our data. The *Cre*$^{+}$ *Luc*$^{/Luc}$, *Cre*$^{+}$*Ext1*$^{+/-}$ *Luc*$^{/Luc}$, and *Cre*$^{+}$*Ext1*$^{+/-}$*Ext2*$^{+/-}$ *Luc*$^{/Luc}$ mice show increased expression seven days after the 2mm ear punch wound. The *Cre*$^{+}$ *Luc*$^{/Luc}$ mouse increased from total flux of $6.55*10^{6}$ p/s to $1.77*10^{7}$ p/s. The *Cre*$^{+}$*Ext1*$^{+/-}$ *Luc*$^{/Luc}$ mouse increased from $3.28*10^{6}$ p/s to $7.24*10^{6}$ p/s. The *Cre*$^{+}$*Ext2*$^{+/-}$ *Luc*$^{/Luc}$ mouse luminescence stayed relatively the same going from $1.28*10^{8}$ p/s to $1.21*10^{8}$ p/s. However, the *Cre*$^{+}$*Ext1*$^{+/-}$*Ext2*$^{+/-}$ *Luc*$^{/Luc}$ mouse increased from $7.60*10^{6}$ p/s to $1.75*10^{7}$ p/s.

A cohort of mice with various genotypes and the radiance expression pre-wound and every seven days post-wound for four weeks was recorded. The luminescence is heightened in the post-wound images, indicating cartilage regeneration. In addition, the luminescence continues to stay elevated over the course of the month (**Figure 4.4**). One can see that in some images the mice's feet and tails may glow, this is because there is cartilage in these areas of the mice and are hairless. Like all animals, they cannot be monitored continuously, and this radiance is mostly likely a product of injury or use of the limbs that have cartilage regeneration occurring normally. A standard size region of interest (ROI) was used to calculate the luminescence in total flux, photons

per second (**Figure 4.5**). Ideally, there was supposed to be an increase in luminescence for each of the *Cre*$^{+}$ genotypes after the wounding, but no significant phenotype was determined from the data collected.

Another phenotype that was investigated in this mouse model was the rate of wound closure. The FGF signaling pathway maintains *Prrx* expression in the blastema (Satoh, et al., 2011). The protein functions as a transcription coactivator, which causes it to bind to an activator to accelerate transcription (Lv, et al., 2016). When *Prrx* is knocked down, it results in suppression of cellular proliferation and cell migration (Lv, et al., 2016). In addition, many studies using an axolotl salamander have shown *Prrx* expression increased significantly in blastema compared to the control intact skin (Sotah, et al., 2010; 2011). Thus, based on the support from previous literature the *Prrx* gene plays a critical role in regeneration. The quantification of the area of the wound closure over time was calculated (**Figure 4.6**). The area of the wound decreased similarly in all the genotypes and most resulted in a final area of approximately 2mm^2 after 28 days post-wound. Compared to the *K14-Cre^{ER} Ext1$^{f/f}$* mouse model, the wound closure in the *Prrx-Cre^{ER} Rosa26-LSL Luc* mouse model was not significant when compared to the controls.

DISCUSSION

Although the *Prrx-Cre^{ER} Rosa26-LSL Luc* mouse model did not indicate enhanced wound healing, it did give us a better understanding on how cartilage repair occurs after an injury. Since *Prrx* is expressed in masses of mesenchymal cells, also known as blastema, the undifferentiated cells have the capability to develop into other cells as needed for regeneration of a limb or wound (Vogg, et al., 2016). Through IVIS imaging we were able to track the increase of *Prrx* expression after wounding. This indicated that after initial wounding, *Prrx-Cre^{ER}* was recruited to the wound site to assist in the repair process. The elevated expression stayed consistent over four weeks

demonstrating that the wound healing process continues for an extended period of time. To further these findings, the next steps would be to observe the GFP with immunohistochemistry. This would allow us to determine which specific cells are involved in the regeneration and repair. Altogether, the *Prrx-Cre*^{ER} *Rosa26-LSL Luc* mouse model was important because it was able to prove *in vivo* the recruitment of *Prrx* to the site of the wound and provide new information for future studies.

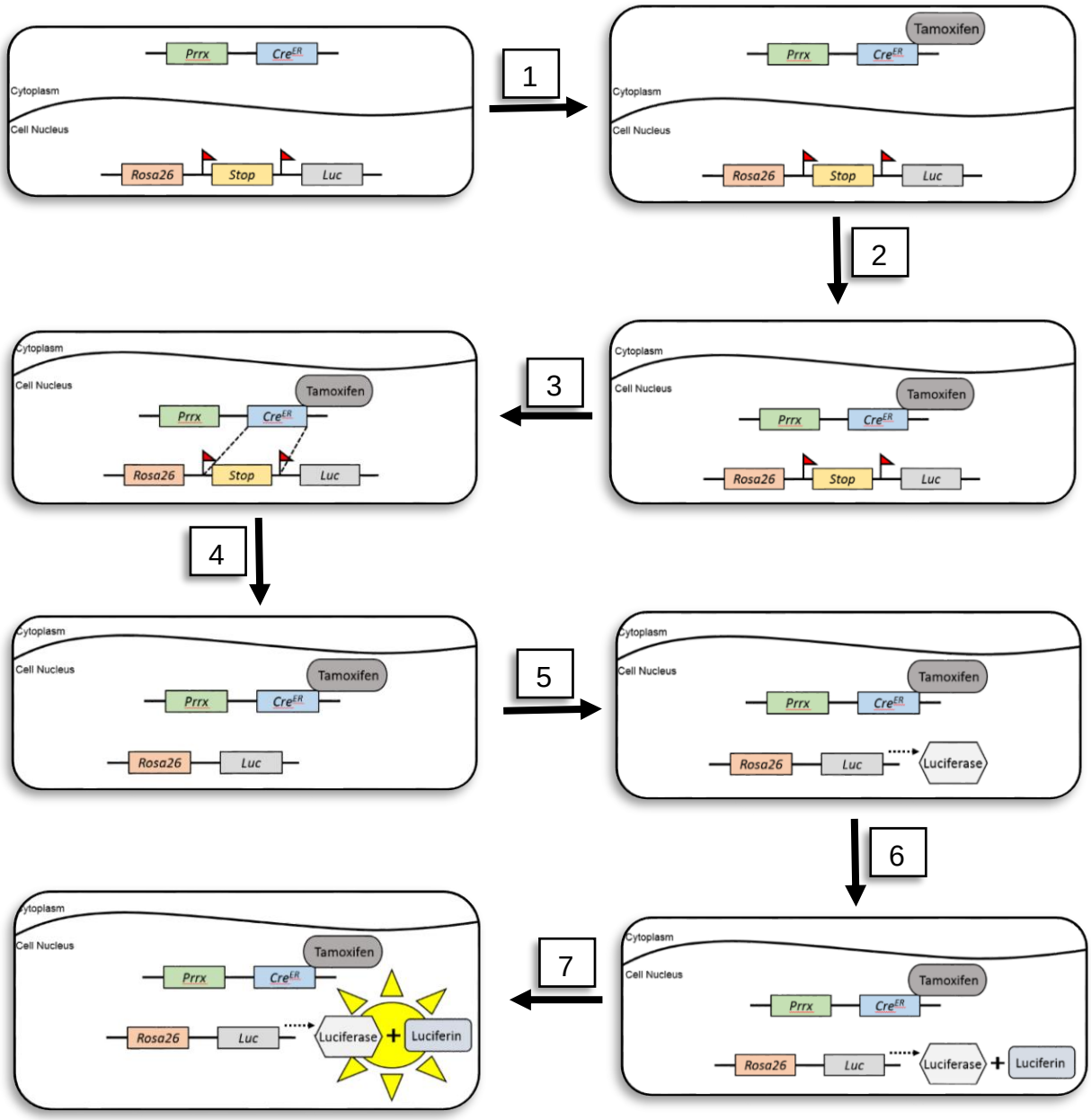

Figure 4.1- Diagram of *Prrx-Cre*^{ER} *Rosa26-LSL-Luc* reporter system.

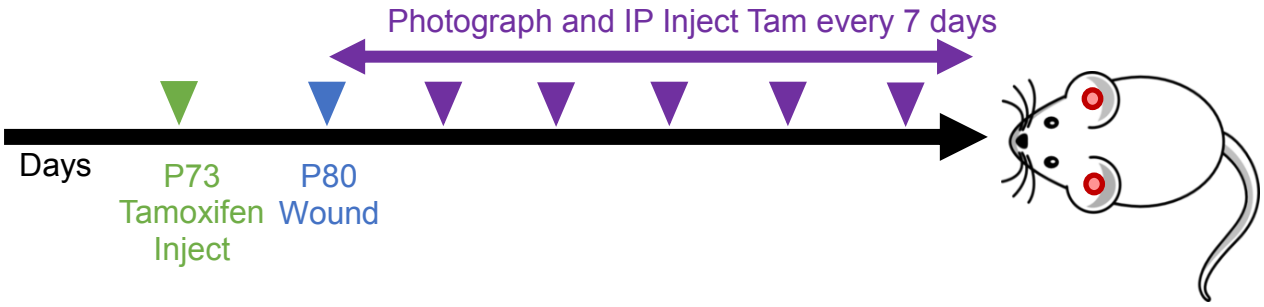

Figure 4.2- Diagram of 2mm ear punch wounding scheme in *Prrx-Cre*^{ER} *Rosa26-LSL-Luc* mouse model.

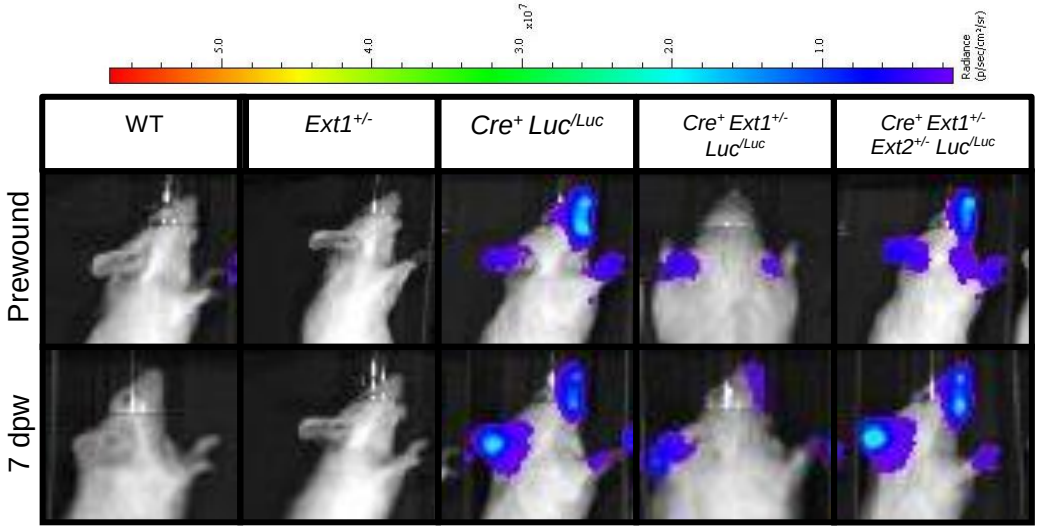

Figure 4.3- Photos of 2mm ear wounds on live animals using IVIS Imaging for luminescence (photons/second); Day 0-7. Various genotypes tested: *Luc$^{/Luc}$*, *Ext1$^{+/-}$ Luc$^{/Luc}$*, *Cre^{+} Luc$^{/Luc}$*, *Cre^{+} Ext1$^{+/-}$ Luc$^{/Luc}$*, *Cre^{+} Ext1$^{+/-}$ Ext2$^{+/-}$ Luc$^{/Luc}$*.

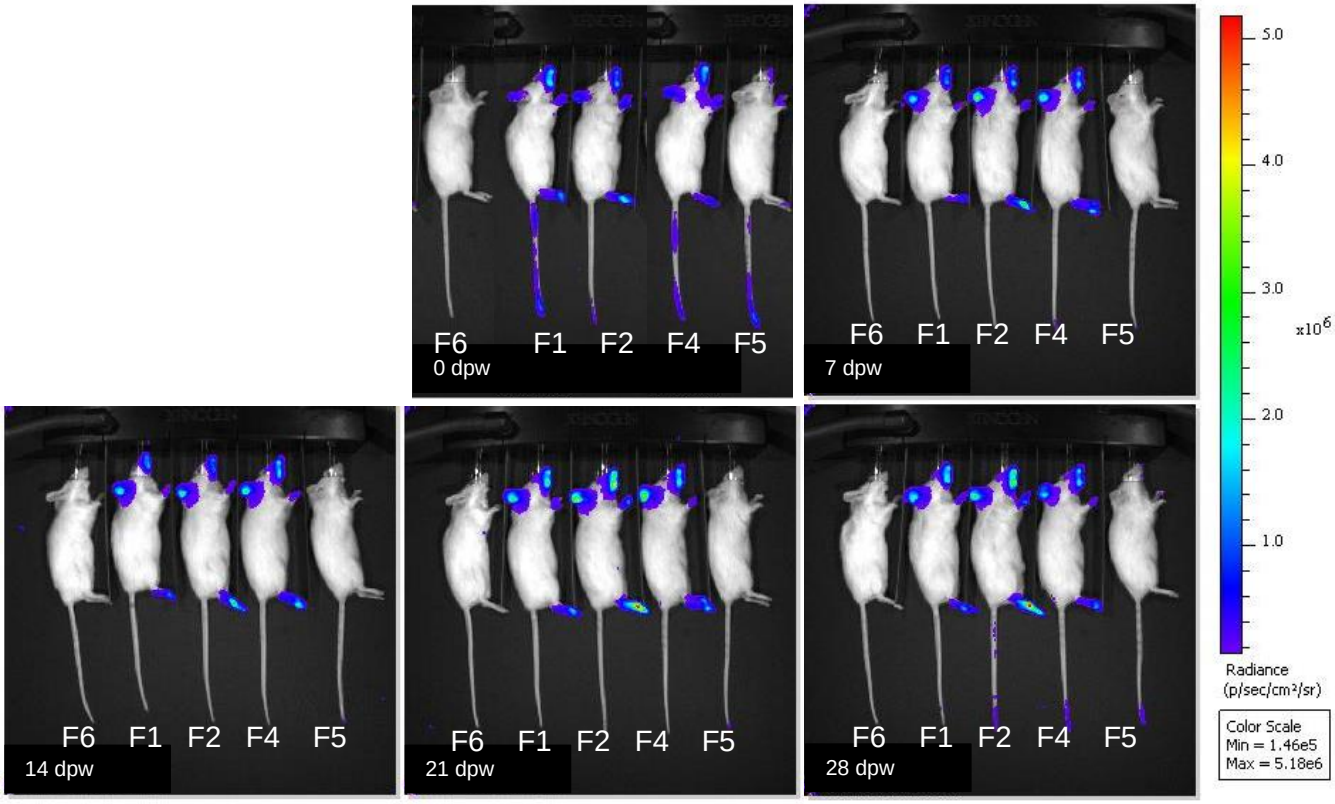

Figure 4.4- Photos of 2mm ear wounds on live animals using IVIS Imaging for luminescence (photons/second); Day 0-28. F1, F2: *Cre*$^{+}$ *Luc*$^{/Luc}$; F4, F5: *Cre*$^{+}$ *Ext1*$^{+/-}$ *Ext2*$^{+/-}$ *Luc*$^{/Luc}$; F6: *Luc*$^{/Luc}$.

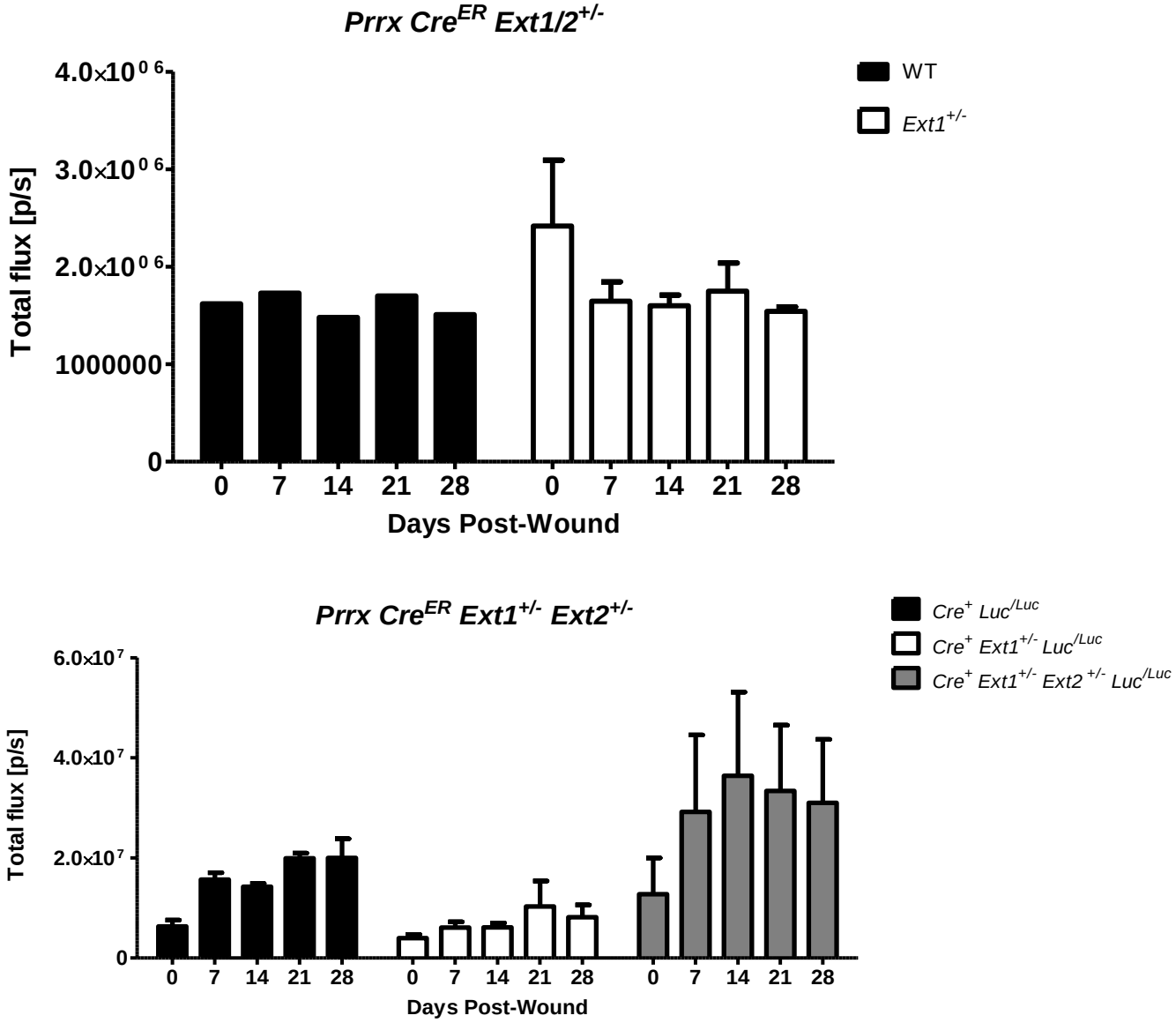

Figure 4.5- Graph of the quantification of ROI data (photons/second) collected from IVIS Imaging; Day 0-28.

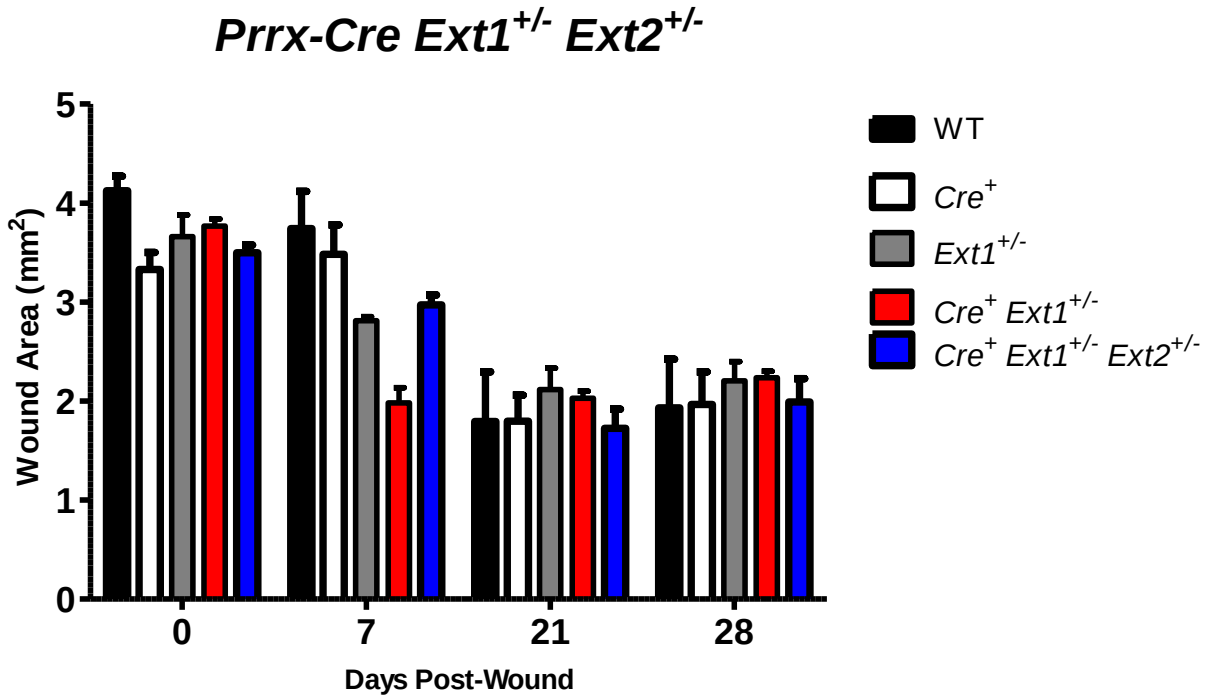

Figure 4.6- Graph of the quantification of 2mm ear wound closure of *Prrx* mouse model; Days post wound 0-28.

CONCLUSION

The objective of this thesis was to test a series of mouse models to determine a genetic or pharmacological method of accelerating the wound healing process. Specifically, we were trying to determine if a mouse model other than the MRL could result in wound regeneration without scarring. The main focus was determining different ways to knockdown heparan sulfate expression because of its role in the three steps of the wound repair process, inflammation, proliferation, and remodeling.

First, we investigated the phenotypic effect on regeneration of the $Ext1^{+/-}Ext2^{+/-}$ gene mutation in C57BL/6 mice. The double heterozygous $Ext1^{+/-}$ $Ext2^{+/-}$ has proven to enhance wound healing significantly, observing a difference after only two days post wound. By day four post wound, the $Ext1^{+/-}Ext2^{+/-}$ wounds began to scab and almost completely healed by day ten post wound, whereas the wildtype lagged significantly. Additionally, we were able to prove *in vivo* the heparan sulfate levels in the skin of wildtype and the double heterozygous the $Ext1^{+/-}Ext2^{+/-}$ mice, resulting in a knockdown of more than 50% in the $Ext1^{+/-}Ext2^{+/-}$ mice. A novel finding of the expression of chondroitin sulfate in mouse skin was determined for the first time, ranging between 50 and 60 μg/gram of dry tissue, ensuing very accurate and precise data.

$K14\text{-}Cre^{+}$ $Ext1^{f/f}$ mice showed significant wound repair compared to the $K14\text{-}Cre^{-}$ $Ext1^{f/f}$ mice, resulting in 53.4% wound healing to a 22.7% wound healing, respectively, after 49 days. Not only did the $K14\text{-}Cre^{+}$ $Ext1^{f/f}$ mice have an accelerated repair rate, but there were also the beginning stages of regeneration. Newly formed chondrocytes were identified in the wounded tissue as well as thickening of the perichondrium. Since, K14 protein is used in the biosynthesis of epithelia cells and the microfilaments and microtubules in the cytoskeleton, it is believed the $K14\text{-}Cre^{+}$ $Ext1^{f/f}$ mice healed faster because the ears have a thin layer of cartilage throughout and

epithelial cells making up the epidermis and dermis on either side of the cartilage. Overall, the *K14-Cre*$^{+}$ *Ext1*$^{f/f}$ genetic manipulation had novel findings and proves that regeneration can be achieved in mice.

Although the NMX enhanced wound healing significantly in 6mm diameter dorsal wounds, it was not well translated to the wound healing of the cartilage in the ear. This could be for a number of reasons, however NMX still has promising effects on wound healing. The addition of aglycone to create a more planar configuration, aids in heparan sulfate priming and the addition of the two aromatic rings bound to the xyloside in NMX is believed to allow for more efficient priming of heparan sulfate.

Although the *Prrx-Cre*^{ER} *Rosa26-LSL Luc* mouse model did not indicate enhanced wound healing, it did give us a better understanding on how cartilage repair occurs after an injury. Through IVIS imaging we were able to track the increase of *Prrx* expression after wounding. This indicated that after initial wounding, *Prrx-Cre*^{ER} was recruited to the wound site to assist in the repair process. The elevated expression stayed consistent over four weeks demonstrating that the wound healing process continues for an extended period of time.

As we look towards the future, the question that has still yet to be answered is, "Why the knockdown of heparan sulfate results in enhanced wound repair and regeneration?" One possibility is that heparan sulfate may naturally sequester growth factor activity, and thus if there is less heparan sulfate present, it allows to growth factor activity to be upregulated. However, which growth factor activities are affected by the heparan sulfate deficiency? As stated in the introduction, heparan sulfate acts as a cofactor for many growth factors' signaling. The deficiency may alter FGF-receptor binding or BMP binding to the cell surface. Additionally, TGF-β cytokine activity could be altered by the heparan sulfate deficiency. It would be interesting to determine

which growth factors are directly affected by the loss of heparan sulfate and develop a pharmacological method to enhance wound healing for humans.

Overall, the investigation into the discovery of a mammalian model for wound regeneration caused by the manipulation of heparan sulfate expression, genetically and pharmacologically, did result in some models that had enhanced and accelerated the wound repair and regeneration.

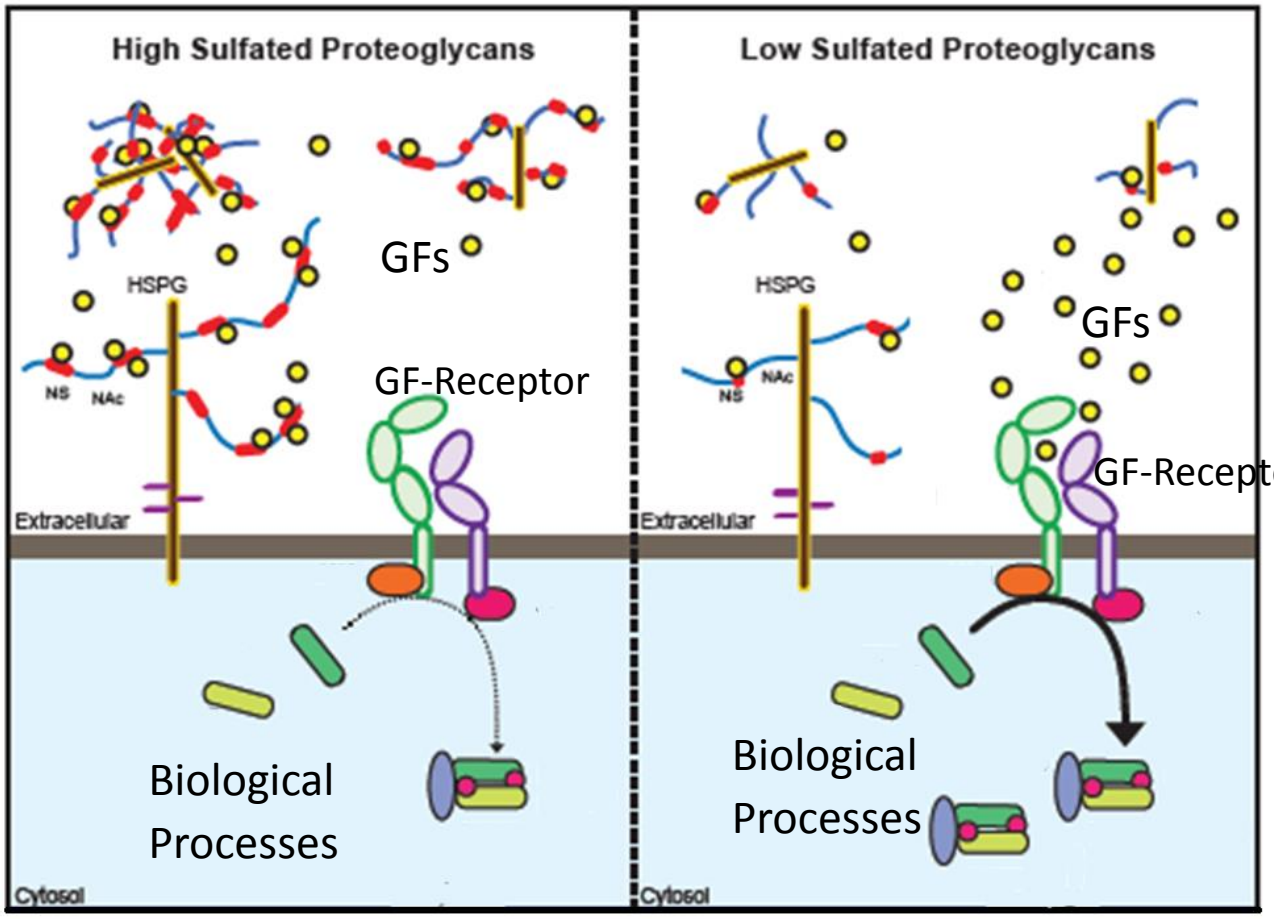

References

Afratis, N.; Gialeli, C.; Nikitovic, D.; Tsegenidis, T.; Karousou, E.; Theocharis, A. D.; Pavão, M. S.; Tzanakakis, G. N.; Karamanos, N. K. Glycosaminoglycans: Key Players in Cancer Cell Biology and Treatment. *FEBS Journal* **2012**, *279* (7), 1177–1197.

Au-Yeung; G.K.; Lu, J.; Moochhala, S.M.; Bay, B.; Yip, G.W. Pathology of wound healing: chondroitin sulfate synthase 1 regulates the expression and activity of caspase 1. *World Medical Conference* **2011**, 222-226.

Barrientos, S.; Stojadinovic, O.; Golinko, M. S.; Brem, H.; Tomic-Canic, M. PERSPECTIVE ARTICLE: Growth Factors and Cytokines in Wound Healing. *Wound Repair and Regeneration* **2008**, *16* (5), 585–601.

Borgens, R. Mice Regrow the Tips of Their Foretoes. *Science* **1982**, *217* (4561), 747–750.

Busse-Wicher, M.; Wicher, K. B.; Kusche-Gullberg, M. The Extostosin Family: Proteins with Many Functions. *Matrix Biology* **2014**, *35*, 25–33.

Canhamero, T.; Garcia, L. V.; Franco, M. D. Acute Inflammation Loci Are Involved in Wound Healing in the Mouse Ear Punch Model. *Advances in Wound Care* **2014**, *3* (9), 582–591.

Cen, Y.; Luo, P.; Liu, X. X. The Effect of Heparin on Wound Healing of Second-Degree Burned Rats. *Zhongguo Xiu Fu Chong Jian Wai Ke Za Zhi* **2000**, *14* (5), 264–267.

Clark, L. D.; Clark, R. K.; Heber-Katz, E. A New Murine Model for Mammalian Wound Repair and Regeneration. *Clinical Immunology and Immunopathology* **1998**, *88* (1), 35–45.

Davis, T. A.; Amare, M.; Naik, S.; Kovalchuk, A. L.; Tadaki, D. Differential Cutaneous Wound Healing in Thermally Injured MRL/MPJ Mice. *Wound Repair and Regeneration* **2007**, *15* (4), 577–588.

Eming, S. A.; Krieg, T.; Davidson, J. M. RETRACTED: Gene Therapy and Wound Healing. *Clinics in Dermatology* **2007**, *25* (1), 79–92.

Fritz, T. A.; Agrawal, P. K.; Esko, J. D.; Krishna, N. Partial Purification and Substrate Specificity of Heparan Sulfate α-N-Acetylglucosaminyltransferase I: Synthesis, NMR Spectroscopic Characterization and in Vitro Assays of Two Aryl Tetrasaccharides. *Glycobiology* **1997**, *7* (5), 587–595.

Fritz, T. A.; Esko, J. D. Xyloside Priming of Glycosaminoglycan Biosynthesis and Inhibition of Proteoglycan Assembly. *Methods in Molecular Biology: Proteoglycan Protocols* **2001**, *171*, 317–323.

Goss, R. J. SECTION III BASIC SCIENCES AND PATHOLOGY 24 Problems of Antlerogenesis. *Clinical Orthopaedics and Related Research* **1970**, *69* (1), 227–238.

Goss, R. J.; Grimes, L. N. Epidermal Downgrowths in Regenerating Rabbit Ear Holes. *Journal of Morphology* **1975**, *146* (4), 533–542.

Gourevitch, D.; Kossenkov, A. V.; Zhang, Y.; Clark, L.; Chang, C.; Showe, L. C.; Heber-Katz, E. Inflammation and Its Correlates in Regenerative Wound Healing: An Alternate Perspective. *Advances in Wound Care* **2014**, *3* (9), 592–603.

Hasty, K. A.; Smith, G. N.; Kang, A. H. Studies on Glycosaminoglycans of Regenerating Rabbit Ear Cartilage. *Developmental Biology* **1981**, *86* (1), 198–205.

Im, A.-R.; Kim, Y. S. Role of Glycosaminoglycans in Wound Healing. *Archives of Pharmaceutical Science and Research* **2009**, *1* (2), 106–114.

Jinno, A.; Park, P. W. Role of Glycosaminoglycans in Infectious Disease. *Methods in Molecular Biology Glycosaminoglycans* **2014**, 567–585.

Kawanami, A.; Matsushita, T.; Chan, Y. Y.; Murakami, S. Mice Expressing GFP and CreER in Osteochondro Progenitor Cells in the Periosteum. *Biochemical and Biophysical Research Communications* **2009**, *386* (3), 477–482.

Kern, G.; Schmidt, M.; Buchner, J.; Jaenicke, R. Glycosylation Inhibits the Interaction of Invertase with the Chaperone GroEL. *FEBS Letters* **1992**, *305* (3), 203–205.

Kim, B.-T.; Kitagawa, H.; Tamura, J.-I.; Saito, T.; Kusche-Gullberg, M.; Lindahl, U.; Sugahara, K. Human Tumor Suppressor EXT Gene Family Members EXTL1 and EXTL3 Encode 1,4- N-Acetylglucosaminyltransferases That Likely Are Involved in Heparan Sulfate/ Heparin Biosynthesis. *Proceedings of the National Academy of Sciences* **2001**, *98* (13), 7176–7181.

Kyritsis, N.; Kizil, C.; Zocher, S.; Kroehne, V.; Kaslin, J.; Freudenreich, D.; Iltzsche, A.; Brand, M. Acute Inflammation Initiates the Regenerative Response in the Adult Zebrafish Brain. *Science* **2012**, *338* (6112), 1353–1356.

Landau, Z.; David, M.; Aviezer, D.; Yayon, A. Heparin-like Inhibitory Activity to Fibroblast Growth Factor-2 in Wound Fluids of Patients with Chronic Skin Ulcers and Its Modulation during Wound Healing. *Wound Repair and Regeneration* **2001**, *9* (4), 323–328.

Ledin, J.; Staatz, W.; Li, J.-P.; Götte, M.; Selleck, S.; Kjellén, L.; Spillmann, D. Heparan Sulfate Structure in Mice with Genetically Modified Heparan Sulfate Production. *Journal of Biological Chemistry* **2004**, *279* (41), 42732–42741.

Leung, T. H.; Snyder, E. R.; Liu, Y.; Wang, J.; Kim, S. K. A Cellular, Molecular, and Pharmacological Basis for Appendage Regeneration in Mice. *Genes & Development* **2015**, *29* (20), 2097–2107.

Li, C.; Pearson, A.; Mcmahon, C. Morphogenetic Mechanisms in the Cyclic Regeneration of Hair Follicles and Deer Antlers from Stem Cells. *BioMed Research International* **2013**, *2013*, 1–21.

Lin, X.; Wei, G.; Shi, Z.; Dryer, L.; Esko, J. D.; Wells, D. E.; Matzuk, M. M. Disruption of Gastrulation and Heparan Sulfate Biosynthesis in EXT1-Deficient Mice. *Developmental Biology* **2000**, *224* (2), 299–311.

Lugemwa, F. N., & Esko, J. D. Estradiol beta-D-xyloside, an efficient primer for heparan sulfate biosynthesis. *The Journal of biological chemistry* **1991**, *266* (11), 6674–6677.

Lv, Z.-D.; Yang, Z.-C.; Liu, X.-P.; Jin, L.-Y.; Dong, Q.; Qu, H.-L.; Li, F.-N.; Kong, B.; Sun, J.; Zhao, J.-J.; Wang, H.-B. Silencing of Prrx1b Suppresses Cellular Proliferation, Migration, Invasion and Epithelial-Mesenchymal Transition in Triple-Negative Breast Cancer. *Journal of Cellular and Molecular Medicine* **2016**, *20* (9), 1640–1650.

Metcalfe, A. D.; Willis, H.; Beare, A.; Ferguson, M. W. J. Characterizing Regeneration in the Vertebrate Ear. *Journal of Anatomy* **2006**, *209* (4), 439–446.

Miao, H.-Q.; Fritz, T. A.; Esko, J. D.; Zimmermann, J.; Yayon, A.; Vlodavsky, I. Heparan Sulfate Primed on β-D-Xylosides Restores Binding of Basic Fibroblast Growth Factor. *Journal of Cellular Biochemistry* **1995**, *57* (2), 173–184.

Murray, L. A.; Knight, D. A.; Laurent, G. J. Fibroblasts. *Asthma and COPD* **2009**, 193–200.

Nascimento, A.P.; Costa, A.M. Overweight Induced by High-Fat Diet Delays Rat Cutaneous Wound Healing. *British Journal of Nutrition* **2006**, 96, 1069-1077.

Okada, M.; Nadanaka, S.; Shoji, N.; Tamura, J.-I.; Kitagawa, H. Biosynthesis of Heparan Sulfate in EXT1-Deficient Cells. *Biochemical Journal* **2010**, *428* (3), 463–471.

Phan, A. Q.; Lee, J.; Oei, M.; Flath, C.; Hwe, C.; Mariano, R.; Vu, T.; Shu, C.; Dinh, A.; Simkin, J.; Muneokka, K.; Bryant, S. V.; Gardiner, D. M. Positional Information in Axolotl and Mouse Limb Extracellular Matrix Is Mediated via Heparan Sulfate and Fibroblast Growth Factor during Limb Regeneration in the Axolotl (Ambystoma Mexicanum). *Regeneration* **2015**, *2* (4), 182–201.

Rapraeger, A.; Krufka, A.; Olwin, B. Requirement of Heparan Sulfate for BFGF-Mediated Fibroblast Growth and Myoblast Differentiation. *Science* **1991**, *252* (5013), 1705–1708.

Saliba, M. J. Heparin in the Treatment of Burns: a Review. *Burns* **2001**, *27* (4), 349–358.

Sarrazin, S.; Lamanna, W. C.; Esko, J. D. Heparan Sulfate Proteoglycans. *Cold Spring Harbor Perspectives in Biology* **2011**, *3* (7).

Satoh, A.; Cummings, G. M.; Bryant, S. V.; Gardiner, D. M. Neurotrophic Regulation of Fibroblast Dedifferentiation during Limb Skeletal Regeneration in the Axolotl (Ambystoma Mexicanum). *Developmental Biology* **2010**, *337* (2), 444–457.

Satoh, A.; Makanae, A.; Hirata, A.; Satou, Y. Blastema Induction in Aneurogenic State and Prrx-1 Regulation by MMPs and FGFs in Ambystoma Mexicanum Limb Regeneration. *Developmental Biology* **2011**, *355* (2), 263–274.

Semenza, G. L. HIF-1 and Mechanisms of Hypoxia Sensing. *Current Opinion in Cell Biology* **2001**, *13* (2), 167–171.

Shriver, Z.; Liu, D.; Sasisekharan, R. Emerging Views of Heparan Sulfate Glycosaminoglycan Structure/Activity Relationships Modulating Dynamic Biological Functions. *Trends in Cardiovascular Medicine* **2002**, *12* (2), 71–77.

Squarize, C. H.; Castilho, R. M.; Bugge, T. H.; Gutkind, J. S. Accelerated Wound Healing by MTOR Activation in Genetically Defined Mouse Models. *PLoS ONE* **2010**, *5* (5).

Tan, C.; de Noronha, R. G.; Roecker, A. J.; Pyrzynska, B.; Khwaja, F.; Zhang, Z.; Zhang, H.; Teng, Q.; Nicholson, A. C.; Giannakakou, P.; Zhou, W.; Olson, J. J.; Pereira, M. M.; Nicolaou, K. C.; Van Meir, E. G. Identification of a novel small-molecule inhibitor of the hypoxia-inducible factor 1 pathway. *Cancer research* **2005**, *65* (2), 605–612.

Varki, A. D.; Cummings, R. D.; Esko, J. W.; Stanley, P. G.; Hart, G. H.; Aebi, M. H.; Darvill, A. L.; Kinoshita, T. H.; Packer, N.; Prestegard, J.; Schnaar, R.; Seeberger, P. *Essentials of Glycobiology*, 3rd ed.; Cold Spring Harbor laboratory press.: Cold Spring Harbor (N.Y.), 2017.

Vasioukhin, V.; Degenstein, L.; Wise, B.; Fuchs, E. The Magical Touch: Genome Targeting in Epidermal Stem Cells Induced by Tamoxifen Application to Mouse Skin. *Proceedings of the National Academy of Sciences* **1999**, *96* (15), 8551–8556.

Vogg, M. C.; Wenger, Y.; Galliot, B. How Somatic Adult Tissues Develop Organizer Activity. *Current Topics in Developmental Biology Essays on Developmental Biology, Part A* **2016**, *116*, 391–414.

Wei, G.; Bai, X.; Gabb, M. M. G.; Bame, K. J.; Koshy, T. I.; Spear, P. G.; Esko, J. D. Location of the Glucuronosyltransferase Domain in the Heparan Sulfate Copolymerase EXT1 by Analysis of Chinese Hamster Ovary Cell Mutants. *Journal of Biological Chemistry* **2000**, *275*, 27733–27740.

Weidemann, A.; Johnson, R. S. Biology of HIF-1α. *Cell Death & Differentiation* **2008**, *15* (4), 621–627.

Williams, R. S. Cell Cycle Control In The Terminally Differentiated Myocyte. *Cardiology Clinics* **1998**, *16* (4), 739–754.

Zak, B. M.; Schuksz, M.; Koyama, E.; Mundy, C.; Wells, D. E.; Yamaguchi, Y.; Pacifici, M.; Esko, J. D. Compound Heterozygous Loss of Ext1 and Ext2 Is Sufficient for Formation of Multiple Exostoses in Mouse Ribs and Long Bones. *Bone* **2011**, *48* (5), 979–987.

Zhang, X.; Liu, L. X.; Wei, X. F.; Tan, Y. S.; Tong, L.; Chang, R.; Marti, G.; Reinblatt, M.; Harmon, J. W.; Semenza, G. L. Importance of hypoxia-inducible factor 1a in healing of burn wounds in a murine model. *Wound Repair Regeneration* **2009**, *17* (A87).

Zhang, Y.; Sheng, Q. S.; Wang, H. K.; Lv, L.; Zhang, J.; Chen, J. M.; Xu, H. Triptolide Improves Nerve Regeneration and Functional Recovery Following Crush Injury to Rat Sciatic Nerve. *Neuroscience Letters* **2014**, *561*, 198–202.

Zhang, Y.; Strehin, I.; Bedelbaeva, K.; Gourevitch, D.; Clark, L.; Leferovich, J.; Messersmith, P. B.; Heber-Katz, E. Drug-Induced Regeneration in Adult Mice. *Science Translational Medicine* **2015**, *7* (290).

Zhou, Z.; Wang, J.; Cao, R.; Morita, H.; Soininen, R.; Chan, K. M.; Liu, B.; Cao, Y.; Tryggvason, K. Impaired Angiogenesis, Delayed Wound Healing and Retarded Tumor Growth in Perlecan Heparan Sulfate-Deficient Mice. *Cancer Research* **2004**, *64* (14), 4699–4702.

Zimmermann, A. S.; Morrison, S. D.; Hu, M. S.; Li, S.; Nauta, A.; Sorkin, M.; Meyer, N. P.; Walmsley, G. G.; Maan, Z. N.; Chan, D. A.; Gurtner, G. C.; Giaccia, A.J.; Longaker, M.T. Epidermal or Dermal Specific Knockout of PHD-2 Enhances Wound Healing and Minimizes Ischemic Injury. *PLoS ONE* **2014**, *9* (4).

Zou, X.; Foong, W.; Cao, T.; Bay, B.; Ouyang, H.; Yip, G. Chondroitin Sulfate in Palatal Wound Healing. *Journal of Dental Research* **2004**, *83* (11), 880–885.

Zou, X. H.; Jiang, Y. Z.; Zhang, G. R.; Jin, H. M.; Hieu, N. T. M.; Ouyang, H. W. Specific Interactions between Human Fibroblasts and Particular Chondroitin Sulfate Molecules for Wound Healing. *Acta Biomaterialia* **2009**, *5* (5), 1588–1595.